

Review

Demystifying the Potential of Anode-Less Alkali Metal Batteries: Uncovering the Role of Liquid and Solid Electrolyte Combinations

Shruti Kannan and Ananthakumar Ramadoss *

Advanced Research School for Technology & Product Simulation (ARSTPS), School for Advanced Research in Petrochemicals (SARP), Central Institute of Petrochemicals Engineering & Technology (CIPET), T.V.K. Industrial Estate, Guindy, Chennai 600032, India

* Correspondence: ananth@cipet.gov.in or ananth.cipet@gmail.com; Tel.: +91-8895001133

How To Cite: Kannan, S.; Ramadoss, A. Demystifying the Potential of Anode-Less Alkali Metal Batteries: Uncovering the Role of Liquid and Solid Electrolyte Combinations. *Materials and Sustainability* 2025, 1(1), 4. <https://doi.org/10.53941/matsus.2025.100004>.

Received: 14 November 2024

Revised: 1 January 2025

Accepted: 23 January 2025

Published: 11 February 2025

Abstract: Contribution to sustainable energy can be effectively routed to decarbonise power generation and transport sectors, by increasing the need for electrochemical energy storage devices such as batteries which can endow greater energy density, longevity, and safety to portable electronic devices. Particularly, anode-less alkali metal batteries (ALAMBs) are promising owing to their cost-effectiveness, and ease of manufacturing, and utilizing a host anode renders the system with recoupable gravimetric and volumetric energy densities. However, interfacial contact resistance, limited ionic pathways, and the formation of dead alkali metals contribute to reduced cation utilization during repeated cycling, which diminishes the system's long-term performance and practical viability. In response, various strategies to optimize the deposition substrate, such as the anodic current collector, interface, and electrolyte have been suggested to prolong the cell lifespan. Most of these approaches are still largely empirical and lack comprehensive diagnostic tools to unravel the complex relationship between the structural changes in the cathode and the nature of alkali metal deposition. This review provides a comprehensive summary of the contemporary improvements carried out in the design and engineering of ALAMBs highlighting the moderation approaches involving both liquid and solid electrolytes to enhance the cycle life, and safety greatly. Finally, the compensatory effects with prospects into the cycling protocols to realize the true energy density of the system are also systematically outlined.

Keywords: anode-less alkali metal batteries; current collector; interface; liquid electrolyte; solid electrolyte; high energy density

1. Introduction

Unprecedented development of highly energy-dense rechargeable batteries could drive the electrification of the transport sector to build a carbon-neutral economy by 2050 [1]. In particular, the emergence of alkali-metal batteries (AMBs) such as lithium-ion batteries (LIBs), sodium-ion batteries (SIBs), and potassium-ion batteries (PIBs) have met the commercialization demands of society, owing to greater specific capacities and lower reduction potentials offered by their metal anodes [2]. LIBs, one of the predominantly used AMBs have achieved energy densities (EDs) only in the range of 250–300 Wh kg⁻¹ when graphite is being used as the anode, while SIBs deliver 90–160 Wh kg⁻¹ of ED when paired with hard carbon anodes at the cell level [3,4]. This restricts their deployment in electric mobility applications. As the technologies mature, the need to explore alternative high E.D. electrode materials are considered significant in augmenting the performance metrics of the AMBs as a whole [5]. Though utilizing alloy (Si, Ge, Sn, Al), conversion (TMO), and metal chalcogenide (TMC, TMN, TMS)-based



Copyright: © 2025 by the authors. This is an open access article under the terms and conditions of the Creative Commons Attribution (CC BY) license (<https://creativecommons.org/licenses/by/4.0/>).

Publisher's Note: Scilight stays neutral with regard to jurisdictional claims in published maps and institutional affiliations.

anodes has enhanced the E.D. of AMBs to some extent, the specific capacity rendered by the alkali metal anodes such as Li: 3860 mAhg⁻¹; Na: 1166 mAhg⁻¹; K: 685 mAhg⁻¹ accompanied by their lower redox potentials of -3.04 V vs. SHE for Li⁺/Li, -2.71 V vs. SHE for Na⁺/Na, and -2.93 V vs. SHE for K⁺/K has spurred the quest for realizing energy-dense batteries [6].

However, these ideal alkali metal anodes suffer from inevitable volume changes and reactivity that induce dendrite growth and a solid electrolyte interface (SEI) that is quite unstable resulting in reduced coulombic efficiency (C.E.), and deprived cyclic stability of the AMBs [7]. Additionally, the alkali metal ion plating/stripping behaviour during charge/discharge greatly impacts cyclic reversibility, with parasitic side reactions causing electrolytic decomposition [8, 9]. To compensate for the alkali-metal ion loss during these side reactions, surplus alkali metal is often used which in turn negates the possibility of achieving higher EDs [10,11]. Relatively, replacing them with thicker alkali metal foils increases the cost of the battery and aggravates safety concerns [12]. On the other hand, producing ultra-thin alkali metal anodes to reduce the thickness requires precise control of the N/P ratio (negative to positive electrode areal capacity ratio), which is demanding and entails careful handling [13]. These issues highlight the need for the progress of ALAMBs, where plain current collectors (CCs) at the negative electrode side are paired with completely lithiated/sodiated/potassiated cathode to achieve the N/P ratio equal to zero, vital for realizing better volumetric/gravimetric EDs with minimal cost from any given cathode system. Furthermore, the requirement of an inert atmosphere is eliminated since the cathodes and electrolytes generally are less reactive, and the alkali metals are formed on the anode only during cell testing [14]. With no excess lithium/sodium/potassium to artificially boost the rate performance, the electrochemical behaviour of ALAMBs mainly relies on the plating/stripping of the alkali metal ions, paving the way for a more accurate performance evaluation of ALAMBs [15,16].

Despite their striking advantages, the realization of ALAMBs is challenging due to reduced coulombic efficiency and cyclic performance. This is essentially ascribed to the energy barrier that impedes the nucleation and growth of alkali metal on the anodic CCs by increasing the nucleation overpotential. This leads to uneven deposition and formation of dead alkali metals [17,18]. Numerous strategies are being proposed to mitigate these issues, and have been reported in various review articles in recent years. Henceforth, this review will provide an overarching understanding of the design, working, and challenges influencing the performance of the ALAMBs. Besides, the manuscript will uncover the recent modification strategies with emphasis on the liquid and solid-state batteries, cycling protocols, compensatory effects, and measures taken to nullify them. Finally, prospects on the emerging technologies and safety concerns to address the irreversible C.E. and cyclic stability will also be highlighted, providing a thorough evaluation of the significance and recurring advancements in the nascent field of ALAMBs.

2. Anode-Less AMBs

2.1. Configuration and Working Mechanism

A typical ALAM full cell does not use a metallic anode during cell assembling. Rather it is in-situ deposited onto the anodic CC during the initial charging, and these cells can effectively deliver an extraordinary E.D. of 500 Wh kg⁻¹ and afar when commercialised. ALAMB comprises an anodic CC which is copper (Cu) for LMB and KMB, whereas SMBs use aluminium (Al) foil instead of Cu to minimize the overall cost of the battery. The other cell components include an electrolyte either in liquid-state or solid-state, a porous polymeric separator in case of a liquid electrolyte, and a fully lithiated/sodiated/potassiated cathode. Considering the example of a Cu||LiMn₂O₄ AL full cell, the first charging process extracts the Li⁺ metal ions from the LiMn₂O₄ cathode and is plated onto the copper CC, where the plated Li⁺ ions react with the electrolyte to form a uniform and stable SEI on the Li metal surface. The lack of a host material to house the alkali metal deposited on the CC makes it a “hostless” anode. The plated metal during discharge, is stripped away and intercalated back into the cathode (Figure 1a,b). In addition, the removal of the graphitic anode from a conventional Li-ion cell, which occupies 46.1% of the cell stack thickness and 27.8% of the total stack weight, can boost the gravimetric E.D. of the cell at stack level to 38.5% with 85.5% increase in its corresponding volumetric E.D. respectively [15,19]. The volume changes that occur as a consequence of anode removal, should be greatly accommodated with tailored battery cell/pack designs.

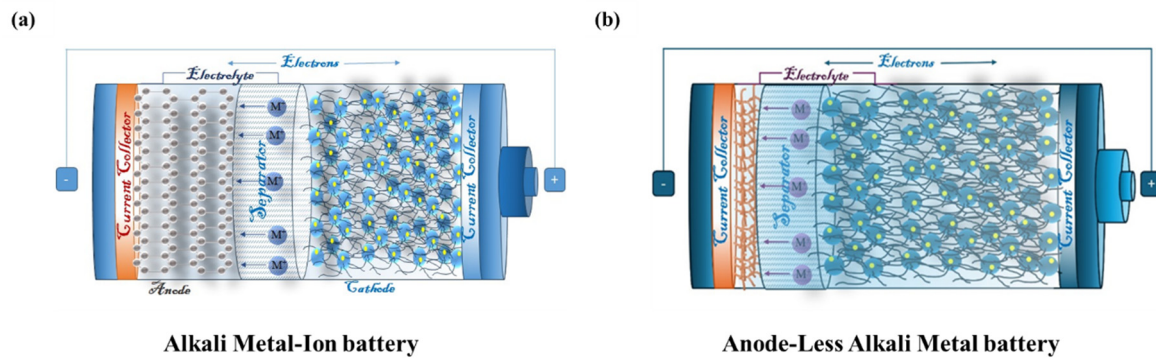


Figure 1. Schematic of the structure and working of (a) conventional AMB and (b) AL-AMB.

These characteristics endow the ALAMBs with the following advantages: **(1) Realistic E.D.**—ALAMBs help to achieve the highest theoretical volumetric E.D. due to its reduced volume, weight and thickness, **(2) Improved Stability**—Overcharge caused by Li/Na/K-based cathodes is greatly alleviated due to the lack of an AM anode. Since the cathodes are completely lithiated/sodiated/potassiated and ALAMBs are assembled in the fully discharged state, their energy state is lower compared to the charged state, as all the metal is delivered by the cathodic system. Furthermore, in the open circuit condition, the reaction is usually non-spontaneous as $\Delta G > 0$, rendering the system with extended stability during repetitive charge/discharge conditions, **(3) Accurate Performance Evaluation**—Alkali metal plating/stripping greatly reflects the precise C.E. of the ALAMB revealing their true behaviour when compared to conventional AMBs, **(4) Cost**—As the use of reactive AM foils is eliminated, the fabrication cost of an ALAMB is highly reduced, and **(5) Safer Handling**—Use of excess alkali metal is avoided, which makes ALAMBs safer to operate [20–22]. This uncovers the possibility of easily integrating ALAMBs into the existing battery production line.

2.2. Challenges in ALAMB Fabrication

Due to subpar electrochemical performance, ALAMBs were once thought to be impracticable. However, the following issues are currently being resolved progressively with promising real-world applications: **(1) Inhomogeneous Alkali-Metal Nucleation and Massive Volume Changes**—Alkali-metal deposition onto the anodic CCs is achieved only when the nucleation and growth barriers are overcome by the larger nucleation overpotentials of AMs. The growth of severe mossy or dendritic structures, produces uneven deposition morphology with the dead Li/Na/K ion formation, triggering severe loss of alkali metal. This instigates electrolytic decomposition due to the heightened side reaction of the generated dead alkali metal with the electrolyte, resulting in rapid volume changes. The sustained growth of these dendritic structures may infiltrate the separator and induce short circuits, degrading the performance of the cell, **(2) Deprived Cycling Stability**—During extended cycling, side reaction-induced structural degradation at the grain boundaries of the cathode could accelerate the transition metal ion diffusion to form an uneven SEI with higher resistance, initiating interfacial polarization, thereby leading to reduced cyclic performance, and **(3) Rapid AM Inventory Loss**—As the N/P ratio is zero for ALAMBs, the amount of usable Li/Na/K is constrained, and any AM loss caused during AM plating/stripping would be due to enlarged stress accumulation at the interfaces. This endows the cell with poor irreversibility of the AM and is true for bare CCs with electrolytes being unoptimized. This inflates the performance of the ALAMBs greatly [15,19, 23–25].

These challenges can be effectuated by incorporating novel methodologies where volume change can be greatly suppressed by appropriating the cell stack pressure accompanied by greater temperature control to regulate the uniform nucleation of AMs. Moreover, employing a three-dimensional (3D) host CC to accommodate the deposited AM could greatly alleviate the volume changes. This requires consideration, as excess electrolytes would be necessary for facile cell operation. Many such approaches are summarized as under:

3. Moderation Approaches

3.1. Tailored Current Collector Design

3.1.1. Anode-Less Lithium Metal Batteries

Regulation of the nucleation-deposition and growth behaviour of alkali metals at the host CC surface is indispensable in improving the cyclability of ALAMBs. The solubility, reactivity, and affinity of Li/Na/K metals

at the heterogeneous interface of the CC make their deposition entirely different [26]. This is due to the lattice mismatch between the AMs and the conventionally used CCs that induces a large interfacial barrier for the transmission of AM ions, which in turn increases their deposition overpotential [27]. Further, the non-alkaliphilic nature of the CC paramountly leads to excessive dead AM formation. This behaviour is majorly impacted by the rate of nucleation/growth, the number of nucleation sites, and the nucleation interplay of AM ions. Thus the stabilization of the CC surface with pre-treatments, coating, and formation of conductive alkaliphilic layers are widely preferred to prevent electrolytic decomposition, with guided AM deposition behaviour, vital for improving the surface homogeneity, C.E., and capacity retention of ALAMBs [28–30]. This section discusses the tailored CC designs focusing primarily on the coatings, and interlayers for the stable cycling of ALAMBs.

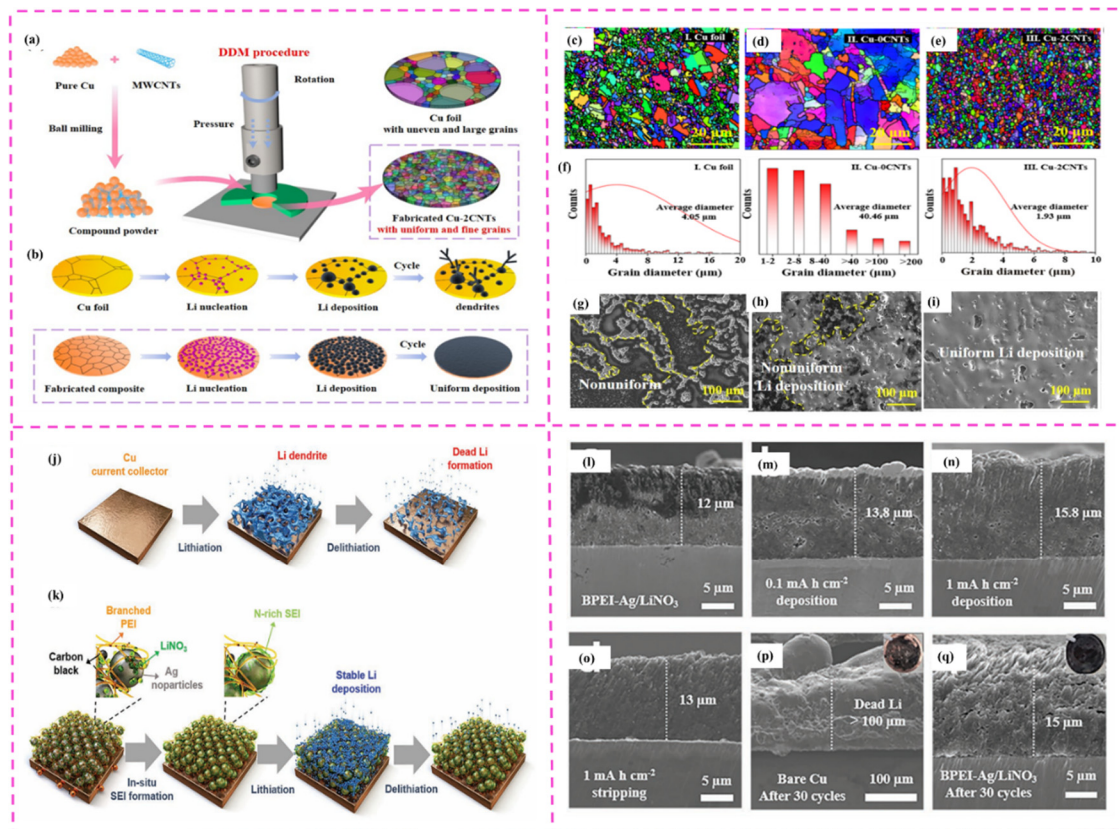


Figure 2. (a) Graphical representation of DDM technique, (b) Li deposition behaviour in bare Cu and Cu-CNT CCs, (c–e) Electron Back Scattered Diffraction (EBSD) images, (f) Average grain diameter, and (g–i) Scanning Electron Microscopy (SEM) images of Li nucleation on the Cu, Cu-0CNTs, and Cu-2CNT CCs. Reproduced with permission from Ref. [31]. Copyright © 2022 Elsevier Ltd., (j) Schematic of Li metal plating and stripping behaviour on bare Cu CC, and (k) BPEI-Ag/LiNO₃ coated Cu CC, Cross-sectional SEM micrographs of BPEI-Ag/LiNO₃ by ion-milling on the Cu CC at 0.1 mA cm⁻² of current density (l) before cycling, after depositing for (m) 0.1 mAh cm⁻², (n) 1 mAh cm⁻², and stripping at (o) 1 mAh cm⁻². Cross-sectional SEM images of de-assembled Li from (p) bare Cu CC, and (q) BPEI-Ag/LiNO₃ at 0.1 mA cm⁻². Reproduced with permission from Ref. [32]. Copyright © 2022 Wiley-VCH GmbH.

Alongside surface modification, achieving uniform grain distribution can enhance the surface area of the Cu CC, suitable for alleviating volume expansion that occurs during charge/discharge cycles of the ALAMBs. The deformation derived morphology (DDM) technique (Figure 2a,b) as proposed by Shan and co-workers owing to its superior plastic deformability was helpful in uniformly distributing carbon nanotubes (CNTs) throughout the Cu matrix. This increased the defect density and engendered the system with more Li nucleation sites, regulating the deposition behaviour of Li onto the Cu CC (Figure 2c–i). The as-prepared Cu-CNT CC when assembled with the LiFePO₄ (LFP) cathode retained 69.4% of its capacity after 100 cycles at 0.5 C and was essential in improving the alkaliphilic nature of the CC [31]. Lithiophilicity can be further improved by assimilating LiNO₃ additives into the electrolyte which was accomplished by erecting a branched polyethyleneimine-silver/lithium nitrate (BPEI-Ag/LiNO₃) electrode onto the Cu CC, which during cycling forms a stable SEI layer, and improves the cyclic stability of the cell (Figure 2j,k). Analysing the Li deposition morphologies at the BPEI-Ag/LiNO₃ electrode at varied current densities is indicative of the fact that the electrode cycled stably with only a mere increase in

thickness even after 30 cycles of plating and stripping (Figure 2l–q). Due to the lipophilic nature of Ag, the BPEI-Ag/LiNO₃ electrode||NCM cell displayed ~99% of C.E. demonstrating around 52% capacity retention after 100 stable cycles [32]. Meanwhile, introducing alkaliphilic sites onto the CC can eventually increase the overpotential leading to the formation of dead AM. This was addressed by introducing zinc into the heteroatom-doped carbon layers on the Cu CC to form Zn@NC@RGO@Cu. The synergy between lithiophilic zinc and carbon layers effectually reduced the overpotential, regulating the nucleation and formation of a dense and uniform Li-plated CC. The modified CC when assembled in LFP||Li@Zn@NC@RGO@Cu cell exhibited a discharge capacity of 152.4 and 103 mAh g⁻¹ at the 5th and 200th cycles of operation. Also, the cell delivered 518 Wh kg⁻¹ of E.D. retaining 89.7% of its capacity at 0.6 C/1 C at room temperature. Moreover, when cycling the cell from 0.1 C to 5 C, 74.3% of rate capability was achieved making it a viable cell combination for use in energy storage systems [33]. Conversely, hosting carbon materials can aggravate the non-uniform Li concentration gradient. Particularly, the use of nanocarbon-based materials [34,35] has gained prominence and inhomogeneous Li deposition was overcome by embedding SiO₂ nanoparticles into the nano carbon-based 3D graphene matrix (Figure 3a) for the Cu current collector at the interfaces, which induces superhydrophilicity (Figure 3b) for Li nucleation. The SiO₂ coordinated 3D carbon network cycled stably with uniform Li deposition behaviour enabling swift kinetics of Li ions, thereby achieving ~98% of C.E. after 100 half-cell operational cycles (Figure 3c–g) [36]. Thus lithiophilic metals incorporated in CCs can better hinder the Li dendrite growth, improve the cyclic performance and are effectual in maintaining the mechanical robustness of the CC greatly.

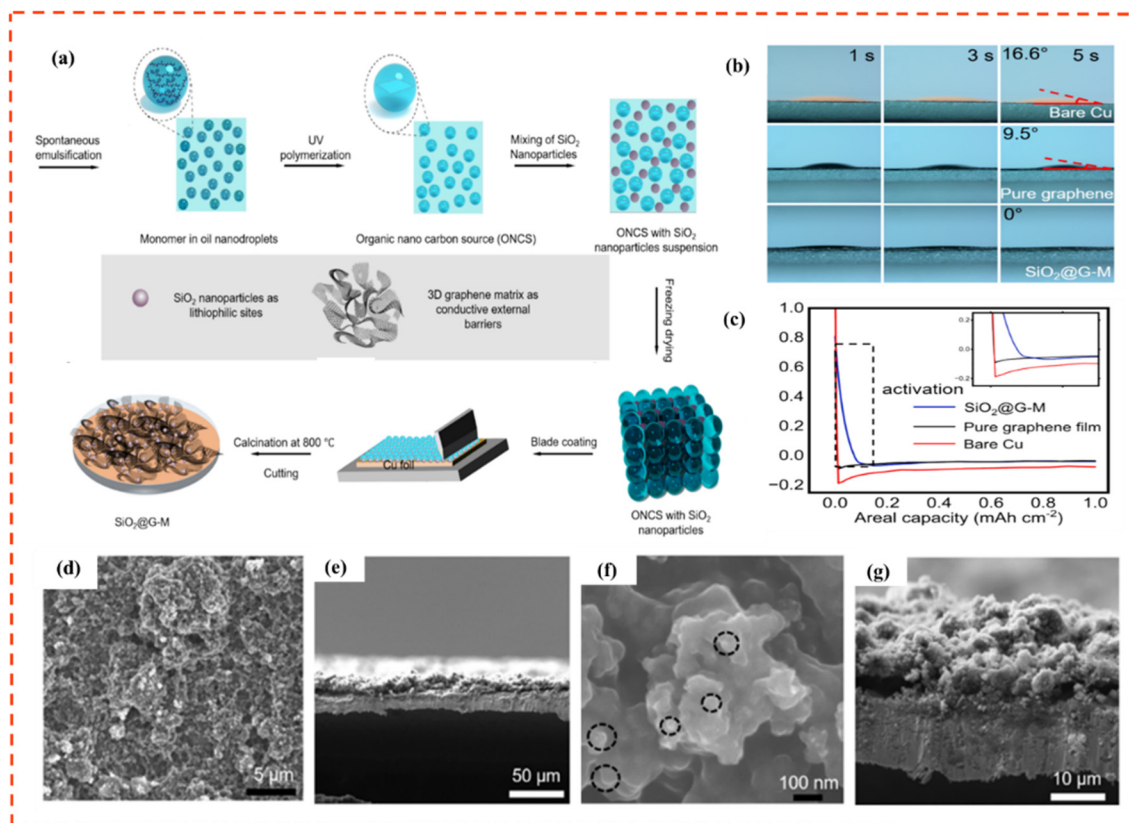


Figure 3. (a) Synthesis and fabrication of SiO₂@G-MCu CC, (b) Electrolyte wettability tests, and (c) Voltage curves of blank Cu, graphene and SiO₂@G-M CCs, (d–g) SEM, and cross-sectional SEM images of SiO₂@G-M CC. Reproduced with permission from Ref. [36]. Copyright © 2024 Elsevier Inc.

Though utilizing tailored 3D CCs reduces the volume expansion, and the localized current density during plating/stripping, their surface area tends to decompose the electrolyte leading to the formation of a less-stable and thick SEI layer worsening the AM ion diffusion and kinetics greatly. This requires electronic structure tuning to balance the formation of the SEI, which has a direct hand in enhancing the AM plating/stripping behaviour. A low-fermi level CC composed of carbon nanofibre (CNF) with Zn-N_x bonds was fabricated to overpower the transfer of electrons from the CC to the LUMO (lowest unoccupied molecular orbital) of the electrolyte (Figure 4a,b). This forms a stable and delicate SEI layer that prevents electrolytic decomposition, and dendritic growth of Li at greater current densities to achieve a capacity of 155 mAh g⁻¹ at 0.5 C, and the full cell combination with Zn-N-CNF||LFP retained 91% of its capacity at 0.5C with a cell E.D. of 495 Wh kg⁻¹

respectively (Figure 4c–e) [37]. Meanwhile, functionalizing the 3D Cu or Ni foam with lithiophilic metals in enhancing the C.E., and E.D. of the cell also poses a great challenge. This prompted the introduction of an extremely thin and lightweight 3D porous Cu CC with subsequent phosphorization to form Cu₄₀@Cu₃P. Compared to pristine Cu CC, where mossy Li deposits appear with cycling, Cu₄₀@Cu₃P exhibits a homogeneous Li deposition, due to their uniformly distributed porosity vital for handling the intrinsic stress and volume changes respectively (Figure 5A(a–o)). The AL-LMB assembled with Li predeposited Cu₄₀@Cu₃P and LFP in both coin and pouch cell prototypes displayed a C.E. of 98.64% with a greater capacity retention rate (Figure 5B(a)), and this is owed to the rational design of 3D CCs with repressed Li metal loss to validate their use in high E.D. applications [38]. Furthermore, a flexible 3D Cu CC with CNT was erected to achieve a high Li⁺ transference number accompanied by an increase in ionic conductivity. Thus the as-erected mechanically stable Cu-CNF displayed an improved Li plating/stripping efficiency and when used in an AL-LMB retained 33% of its initial capacity than the pristine Cu CCs [39]. Consequently, Li plating/stripping is highly impacted by the volume changes that are inherent due to Li metal dendrite growth. Deng et al. addressed this by devising a breathable 3D Li host consisting of MnO₂ nanoflakes to improve the reversibility of Li metal ions during the plating/stripping process. It was observed that the fabricated hierarchical 3D structure accommodated large volume changes and possessed a dendrite-free structure even at 10 mAh cm⁻² [40].

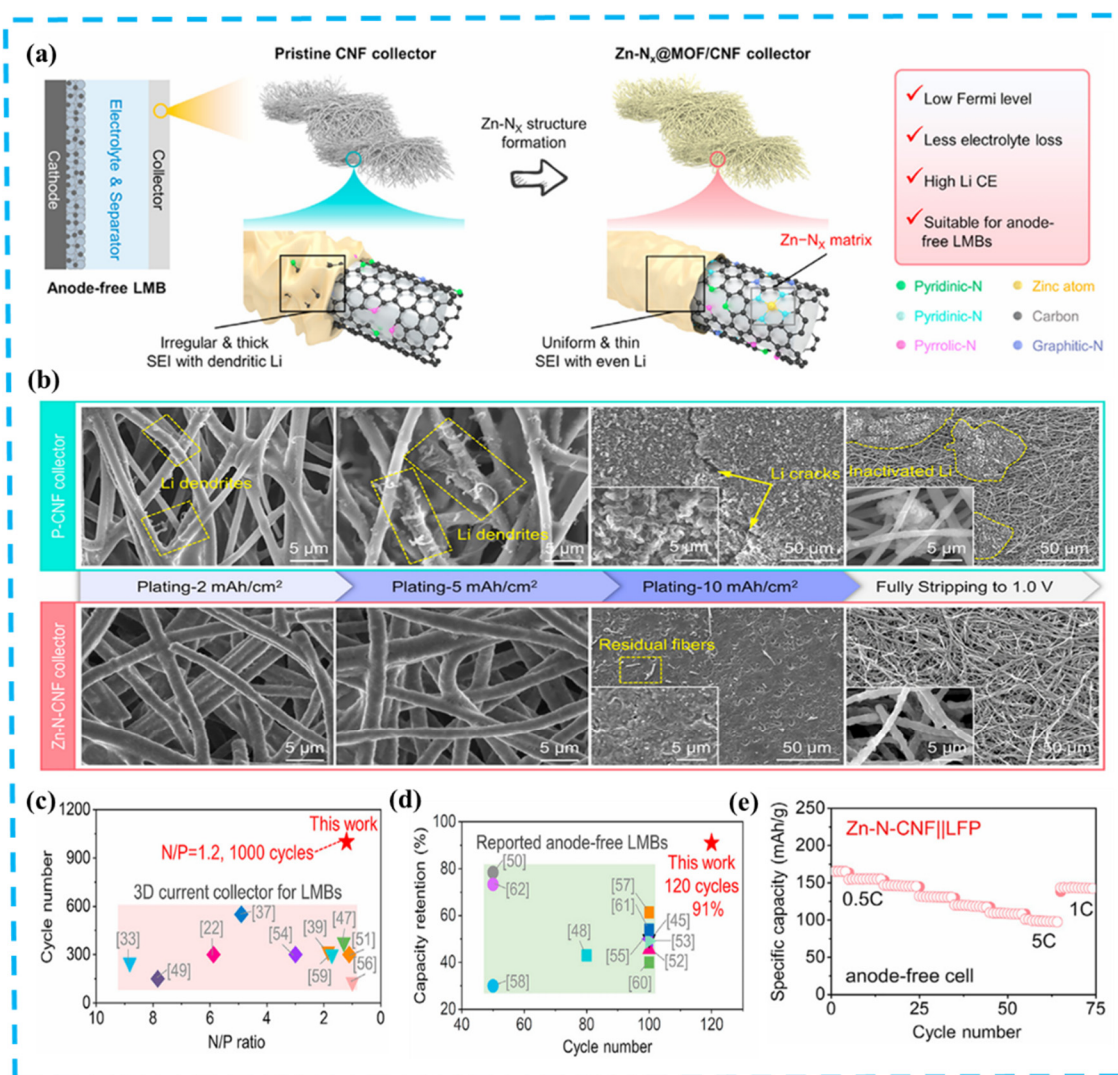


Figure 4. (a) Pictorial representation of the fabrication of Zn-N@MOF/CNF CC, (b) SEM micrographs of P-CNF and Zn-N@MOF/CNF CC, Electrochemical behaviour of (c) Li/Zn-N-CNF||LFP, and (d) Zn-N-CNF||LFP cells, (e) Rate capability of Zn-N-CNF||LFP cells. Reproduced with permission from Ref. [37]. Copyright © 2023 Elsevier Inc.

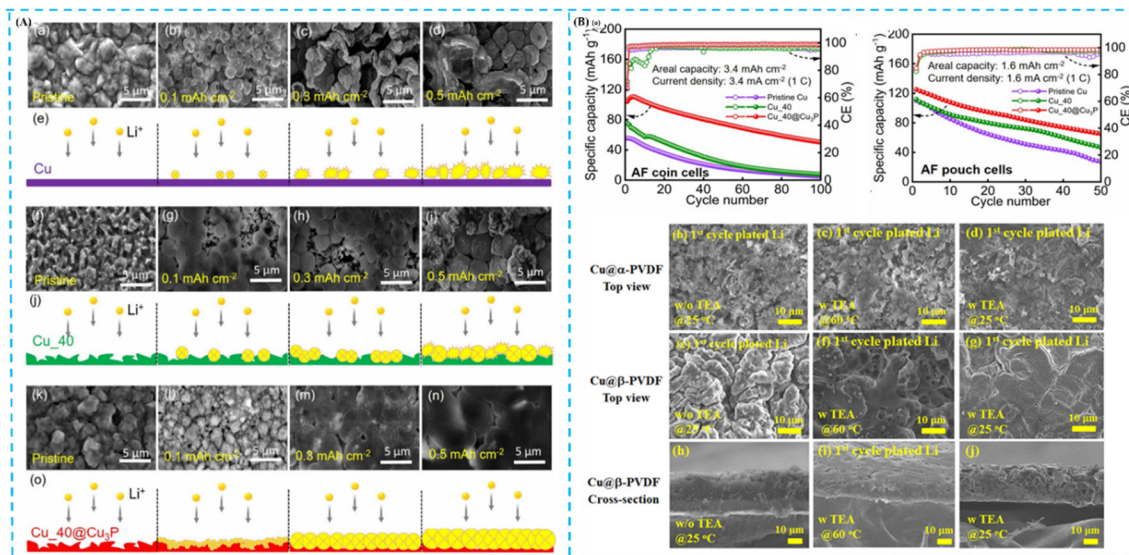


Figure 5. (A) (a) SEM micrographs of evolution of morphology during Li nucleation on (a–e) bare Cu, (f–j) Cu₄₀, (k–o) Cu₄₀@Cu₃P at varied capacities of 0.1 mAh cm⁻², 0.3 mAh cm⁻², and 0.5 mAh cm⁻². (B) (a) Cyclic performance of Cu||LFP, Cu₄₀||LFP, and Cu₄₀@Cu₃P||LFP AF coin cells at 1 C, and Cu||LFP, Cu₄₀||LFP, and Cu₄₀@Cu₃P||LFP AF pouch cells. Reproduced with permission from Ref. [38]. Copyright © 2024 American Chemical Society, (b–j) SEM images of Li plating on Cu@ α -PVDF, and Cu@ β -PVDF at 0.25 mA cm⁻². Reproduced with permission from Ref. [45]. Copyright © 2021 American Chemical Society.

A similar work was reported by Li et al., where gold (Au) nanoparticles combined with rGO (Au/rGO) were used as a deposition host to improve the lithiophilicity of the CC by correspondingly lowering the nucleation barrier. The a-developed Au/rGO film displayed 97% of C.E. at 1 mA cm⁻² even after 500 cycles, and benefitting from this configuration the AF full cell with LFP||Au/rGO exhibited a remarkable capacity retention of 96% even after 100 operational cycles [41]. Realizing dendrite-free deposition can enhance the transport kinetics of Li and this involved the development of a heterogeneous CC with soft and hard base structures (HBSA-Co CC) facilitating smooth Li deposition by lowering the nucleation barrier. The HBSA-Co CC||NCM811 full cell delivered 209.2 mAh g⁻¹ of specific capacity at 3.8V and retained nearly 78.9% of its initial capacity after 150 stable cycles. This was contrasted theoretically proving the efficacy of soft HBSA-Co CCs in the reduction of Li metal nucleation/growth barriers [42]. Meanwhile, the introduction of a high entropy alloy such as CuInNiSnCd onto the 3D carbon fibre host can augment the number of active lithiophilic sites, alleviate the volume expansion, and aid in swift Li⁺ transport. The half-cell configuration with HEA/CF resulted in localized Li flux and exhibited 99.5% of C.E. at a charge/discharge capacity of 2 mAh cm⁻²/1 mAh cm⁻² respectively. The as-spun HEA/CF when paired with NCM811 cathode showed a stable cycling performance with a C.E. of 99.2% at 1 C after 160 cycles of operation [43]. More recently, the effect of bipolar composite CCs (BCCC) on the electron transfer behaviour was studied by Liao et al., where extremely thin asymmetric Cu and Al were deposited on both sides of polyethylene terephthalate (PET) substrate. The as-prepared CCC when integrated into the AF pouch cell displayed 99.1% of C.E. and retained 50% of its capacity after 100 cycles, proving it as a potential alternative to the conventional CCs [44].

Coating the CC surface is also a promising option as they are operational in reducing the interfacial resistance caused by the direct contact of AM deposits and the electrolyte. This can be attributed to the fact that the artificial coating of the SEI layer on the CC, can be tuned to desired composition and structure, and is defect-free to tolerate the extreme volume changes that occur during cycling. In this regard, polymeric β -phase PVDF was conformally used as a beneficial coating layer on Cu by electrospinning, as its adsorption energy was effective in directing the Li flux, which stimulates the development of LiF-rich SEI during continuous Li plating/stripping. The Cu@ β -PVDF fibre which underwent thermal-electrochemical activation (TEA) exhibited a smooth Li deposition morphology notably at 25 and 60 °C, even after stripping for 30 consecutive cycles to improve the electrochemical performance (Figure 5B(b–j)). The Cu@ β -PVDF||NMC cell with TEA cycled stably achieving 68.36% and 78.45% of C.E. at 25 and 60 °C respectively [45]. These CC coatings often lead to irreversible AM ion loss during the initial stages of cycling. This was overcome by electroless plating of Cu and silver (Ag) onto the delicate low-dust paper-based (LDP) CC. The as-prepared LDP-based CCs showed increased lithiophilicity due to their reduced nucleation overpotential of 18.3 mV

and it has been observed that the initial discharge capacities are lower for the fabricated CCs, due to inefficient Li recovery. Hence, regulating the lithiophilicity of CCs by appropriate tuning can imperatively reduce Li loss and facilitate better efficiency [46]. The reduction in initial C.E. was effectively mitigated by epitaxially inducing Li metal layers onto the Cu CC (E-Cu). This operational layer facilitates Li storage by facile alloying, enabling swift diffusion and formation of LiF-based SEI onto the Cu and E-Cu CC (Figure 6a,b). This E-Cu CC enhanced the C.E. and capacity retention of the symmetrical Li cell from 93.24% to 98.24% and 66% to 84% respectively (Figure 6c,d). In addition, benefitting from an E.D. of 420 Wh kg^{-1} , the asymmetric NCM||E-Cu pouch cell configuration makes it attractive for advanced battery-related applications [47].

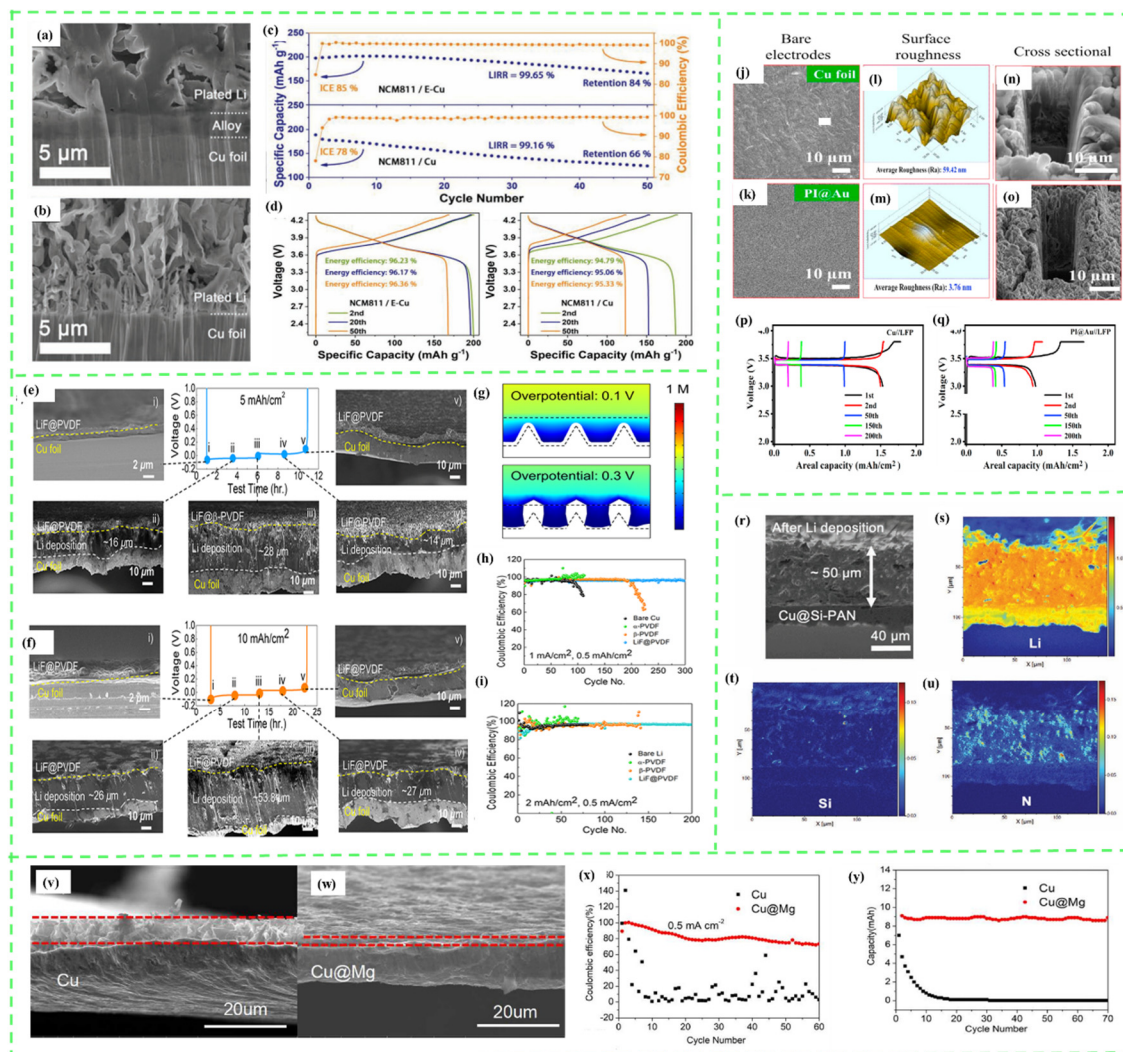


Figure 6. (a,b) Cross-sectional SEM micrographs of E-Cu and Cu CCs after plating Li at 5 mAh cm^{-2} at 0.5 mA cm^{-2} , (c) Cyclic performance, and (d) Voltage curves of NCM811||E-Cu pouch cell at various cycles. Reproduced with permission from Ref. [47]. Copyright © 2021 Wiley-VCH GmbH, (e,f) Plating/stripping of Li at LiF@PVDF with different areal capacities, (g) Simulation depicting the Li concentration gradient with a polymer-coated Cu CC and, (h,i) C.E. of LiF@PVDF at 1 mA cm^{-2} and 2 mA cm^{-2} respectively. Reproduced with permission from Ref. [48]. Copyright © 2021 American Chemical Society, SEM micrographs (j,k) bare Cu foil, (l,m) PI@Au after Li-plating at 2 mAh cm^{-2} at 0.5 mA cm^{-2} . Focused Ion Beam (FIB) images of (n,o) Cu foil and PI@Au at 2 mAh cm^{-2} at 0.5 mA cm^{-2} , Electrochemical performance of (p) Cu||LFP, and (q) PI@Au||LFP at 0.5 mA cm^{-2} . Reproduced with permission from Ref. [49]. Copyright © 2021 Elsevier B.V., (r) Cross-sectional SEM and (s–u) Time of Flight-Secondary Ion Mass Spectroscopy (ToF-SIMS) imaging of Cu@Si-PAN after full charge. Reproduced with permission from Ref. [50]. Copyright © 2022 Wiley-VCH GmbH, (v,w) Cross-sectional SEM images and (x,y) Cyclic performance graphs of Cu and Cu@Mg. Reproduced with permission from Ref. [51]. Copyright © 2024 Elsevier Ltd.

Apart from metals, synergistic effects of polymer/dielectric nanoparticles such as LiF@PVDF can also expedite uniform reversible Li plating and stripping behaviour owed to their reduced overpotential, localized current density, and extended C.E. at fixed cell capacities of 1 mAh cm⁻² and 2mAh cm⁻² respectively (Figure 6e–i) [48]. In addition to improving the cyclic stability, lithiophilic metals tend to cause short-circuiting when Li gets deposited onto the separator. This was addressed by employing a polyimide-based porous insulated CC sputtered with conductive gold (PI@Au). When investigating its suitability as a potential anodic CC, its surface roughness was tested, where the value remained lower (3.76 nm), which was operative in limiting the nucleation barrier enabling guided Li deposition and growth, away from the separator (Figure 6j–o). Besides, the cell with PI@Au||LFP achieved better retention capabilities of 48.4% and 38.6% at the 100th and 200th stable cycles than Cu||LFP (Figure 6p,q), indicating its viability as a potential anodic CC for AL-LMBs [49]. The disadvantages of employing a flammable liquid electrolyte were also channelized by adopting a combination of LNMO cathode with silicon-polyacrylonitrile (Si-PAN) coated CC with a modulated wide-voltage window electrolyte containing 1 wt% of LiTFSI additive which induced homogeneous Li metal growth (Figure 6r–u) during battery cycling [50]. Apart from coatings, the methodology used for coating the CC with lithiophilic metals should also be considered, as they have a direct hand in controlling the thickness and loading of the coated layer. In this regard, Nan et al. erected a dynamic layer of lithiophilic magnesium onto the Cu CC via magnetron sputtering (Figure 6v,w). Subjecting the Mg-coated Cu CC to half-cell tests delivered a C.E. of 83.7% at 0.5 mA cm⁻² after 50 cycles (Figure 6x,y) and the anode-free LFP||Mg-Cu configuration cycled for > 50 cycles, at 1C without significant capacity decay [51]. Thus current collector coatings offer new insights into the design of ALAMB that can endow the cell with extended safety, stability and greater EDs.

3.1.2. Anode-Less Sodium and Potassium Batteries

Despite the enormous development of LIBs in recent decades, their dwindling supplies have aroused the need to look into alternative battery chemistries such as SIBs and PIBs due to their comparable specific capacities, lower redox potentials and heightened flame resistance than lithium. Utilizing potassium and sodium as carrier ions, conventionally used cobalt-based cathodes can be easily replaced with sodium/potassium-based cathodes and cost-effective aluminium current collectors. However, the moisture sensitiveness of the pristine sodium/potassium metal anodes hinders their practicality [52,53]. Yet, AL sodium/potassium metal batteries are still in the nascent stage of development and warrant further investigation. In this regard, a potassiophilic graphene layer was grown in situ onto the Al CC with surface homogeneity via plasma-enhanced chemical vapour deposition (Figure 7(a1,a2)). The graphene-modified CC with an extremely thin layer reflected a better surface morphology than bare Al and Al@C CCs, which aids in jeopardising potassium loss (Figure 7(a3–a5)). The as-assembled Al@G||K-FeS₂ cell displayed an initial C.E. of 73.6% and was able to light an LED (light-emitting diode) in the state of deformation (Figure 7b,c) [54]. A similar work by Cui et al. highlighted the use of incompletely selenized Cu-OSe nanowires as a host for potassium metal nucleation. The Cu-OSe nanowire exhibited good reversibility in a symmetric cell configuration for over 950 h respectively and the anode-free K_{0.5}MnO₂||Cu-OSe NWs cell cycled for over 200 cycles with 63.5% of capacity retention [55]. Further, to effectually hinder the potassium dendrite growth and induce potassiophilicity onto the CCs, a Cu₆Sn₅ layer was electroless plated onto the Cu CC by Ren et al., where the stable KF SEI layer enhanced the stability performance for upto 600 h at a current density of 1 mA cm⁻² respectively [56].

Consequently, the sodium-metal ion reversibility in AF batteries was investigated by introducing nanosized Pb (lead) coating onto the surface of carbon-coated Al CC via magnetron sputtering. Post-cycling, when contrasting the electrochemical behaviour of Pb-Al@C||NVP cell with Al@C||NVP, Pb-Al@C CC was extremely sodiophilic providing a large number of active sites for Na ion nucleation and showed the negligible formation of dead Na even after 100 cycles of operation. Ultimately, the ALSMB with Pb-Al@C||NVP combination, delivered 84.6 mAh g⁻¹ of discharge capacity after 200 cycles with ~99% of C.E. and capacity retention of 81.9% respectively [57]. Regulating the deposition behaviour of Na at greater current densities can have a significant effect on the energy density and safety of the AF sodium metal batteries. This necessitated the construction of a self-supporting MgF₂@NCHNF host, which during cycling transforms into gradient-assisted fluorinated alloy, which was found effective in augmenting of number of sodiophilic sites required for directing the distribution of Na flux. Moreover, the assembled Na-MgF₂@NCHNF||NVP pouch cell, retained 96% of its capacity even after 400 cycles at 2C respectively [58]. Meanwhile, a 3D honeycomb structured bismuth nanosheets were grown vertically on Cu foil by Bai et al., to effectively hinder the volume changes that occur due to greater Na metal reactivity. The half-cell configuration with the fabricated Bi-NAs@Cu displayed higher Na-ion reversibility to

exhibit 99.8% of C.E. at a greater current density and subsequently, ALSIB with $\text{NaTi}_2(\text{PO}_4)_3$ (NTP)||Bi-NAs@Cu exhibited a retention of 93.22% at 1C after 267 cycles proving its potential as a 3D sodium host [59]. Noticeably, to supplement the Na-metal ion inventory loss during cycling, a nucleation buffer layer comprising a Cu-based metal-organic framework (MOF) was proposed to be placed between the cathodic and anodic Al foil CCs. The composite Cu-Cu@C CC enabled smooth Na deposition morphology even at a higher capacity of 6 mAh cm^{-2} , indicating its ability to host large Na metal ions with less change in volume (Figure 7d–j). The cell with NVP cathode and Al-Cu@C CC displayed a discharge capacity of 102 mAh g^{-1} for the initial cycle and a capacity decay is significantly observed after 30 cycles when cycled at 1C during discharge (Figure 7k,l), indicating that an increase in anodic potential would subsequently disrupt the Na-ion reversibility [60]. This entails crucial engineering of functional CCs such as 3D Zn@Al with a porous morphology via the magnetron sputtering method. The 3D Zn@Al CC owing to its better wettability properties allowed for facile Na-ion diffusion which reduced the nucleation overpotential and facilitated proper Na plating/stripping. The modified 3D Zn@Al CC (Figure 7m–t) with the NVP cathode displayed a remarkable capacity retention of 98.11% at 50C even after 2000 cycles of operation proving it highly advantageous for effective Na metal utilization [61]. Similarly, an anode-free configuration of a multivalent-zinc battery with zincophilic antimony (ZA) nanoparticles (ZA@3D-nanoCu) was developed to nullify the zinc dendrite growth. Such ZA@3D-nanoCu CCs in combination with Zn cathode exhibited an enhanced rate performance at a fixed areal capacity of 5 mAh cm^{-2} and their corresponding SEM images revealed a uniform, smooth morphology than Cu CC indicating the structural integrity of the ZA@3D-nanoCu. The full cell with ZA@3D-nanoCu||Br₂ displayed enhanced cyclic stability at an areal capacity of 10 mAh cm^{-2} and retained 400 mAh g^{-1} of specific capacity (96.2%) even after 1000 cycles (Figure 7u–w) validating its robustness for use as anodic CCs in realistic aqueous Zn batteries [62]. However, the alkali metals' high reactivity places severe constraints on the production environment.

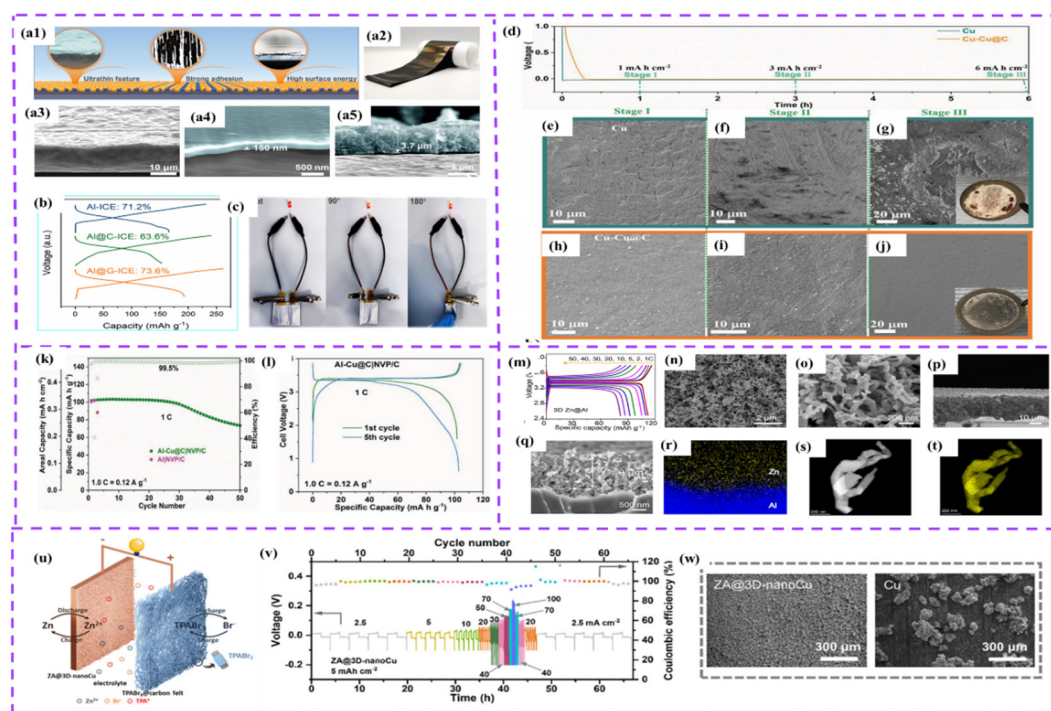


Figure 7. (a1,a2) Pictorial representation of fabricated Al@G and the cross-sectional SEM micrographs of (a3–a5) Al, Al@G, and Al@C, (b) 1st cycle GCD curve of AF K-FeS₂||Al@G, K-FeS₂||Al, and K-FeS₂||Al@C, and (c) LED powered by K-FeS₂||Al@G during bending. Reproduced with permission from Ref. [54]. Copyright © 2022 Wiley-VCH GmbH. (d) Voltage curves of Cu and Cu-Cu@C, SEM images of (e–g) bare Cu, and (h–j) Cu-Cu@C and (inset depicts the images of Cu and Cu-Cu@C after Li plating at 6 mAh cm^{-2}), (k,l) Cyclic performance and discharge profiles of Al-Cu@C||NVP/C, and Al||NVP/C at 1C, Reproduced with permission from Ref. [60]. Copyright © 2022 The Authors. Advanced Energy Materials published by Wiley-VCH GmbH, (m) Charge-discharge curves of 3D Zn@Al||NVP cell, (n–q) SEM, (r) Energy Dispersive X-ray Spectroscopy (EDAX) images of 3D Zn@Al, and (s,t) High-angle Annular Dark-field Imaging (HAADF) of Zn. Reproduced with permission from Ref. [61]. Copyright © 2023 Elsevier Ltd., (u) Representation of ZA@3D-nanoCu||Br₂, (v) Rate performance, and (w) SEM micrographs of ZA@3D-nanoCu at 5 mAh cm^{-2} . Reproduced with permission from Ref. [62]. Copyright © 2023 Elsevier Ltd.

3.2. Balanced Interfacial Chemistry

The thermodynamic energy gap that arises during electrode/electrolyte contact determines the cell voltage. During continuous charge/discharge, there is a subsequent increase/decrease in battery voltage, due to the electrochemical reactions that occur when electrode and electrolyte are in contact. This results in the development of an interface called the SEI on the anode side and CEI (cathode electrolyte interface) on the cathodic side. These interfaces collectively enhance the cyclic stability and longevity of the batteries. However, unwanted side reaction at the electrodes aggravates the formation of unstable SEI and CEI layers, which eventually leads to electrolytic decomposition and accelerates the risk of short circuits [63,64]. This instigates the need to design a balanced interfacial chemistry at the electrode/electrolyte, prominent enough to increase the performance of ALAMBs.

3.2.1. Anode-Less Lithium Batteries

Notably, preloading a Li-based compound on the cathode side can supplement Li and aid in replenishing the irreversible capacity loss. In this context, Qiao et al. preloaded a Li_2O sacrificial agent into NCM (8:1:1) cathodes, whereby O_2^- released from Li_2O during oxidation was indispensable in forming a LiF-based CEI onto the cathode, to passivate the decomposition of the electrolyte. It is evident from the surface-enhanced Raman studies that the LiF layer is completely developed on the NCM cathode, extending the oxidation stability to 4.8 V during Li plating/stripping. Moreover, the AF pouch cell with NCM@ Li_2O cathode and Cu CC could deliver 320 Wh kg^{-1} of E.D. with nearly 80% of its capacity retained after 300 operational cycles [65]. To analyze the effect of pressure on stable SEI layer formation (Figure 8a–c), pure graphene was directly coated onto the Cu CC, which acted as a seed layer to promote Li wetting at a nominal pressure of 1MPa, and underwent single lithiation/delithiation in the voltage range of $50 \mu\text{A cm}^{-2}$. With the development of SEI on pG@Cu, the thickness of $\sim 5 \mu\text{m}$ for pG has been retained and when cycled in the cell configured with the NCM cathode (Figure 8d–f), it delivered an areal capacity of 2.94 mAh cm^{-2} at 0.1C respectively [66]. Besides, the formed unstable SEI due to its disordered structures and generated by-products lowers the ionic conductivity and results in mechanical failure. This was addressed by constructing an artificial SEI layer with the integration of LiPON and LiF, to promote ionic conductivity and lessen the dendrite formation. The synergistic effects of LiF-LiPON lowered the ionic diffusion length and were accompanied by their greater modulus of elasticity to promote a uniform Li deposition morphology (Figure 8g,h). The as-prepared artificial composite SEI layer when paired with Cu CC, LFP, and NCA cathodes retained $>60\%$ (Figure 8i,j) of its capacity after 100 cycles proving its potential for use in practical AL-LMBs [67].

More guided Li deposition can be achieved by artificially inducing a $\text{Li}_{4.4}\text{Sn}$ layer onto the CC, which facilitates an ample amount of interfacial charge transfer to enhance the C.E. and cyclic performance greatly [68]. A similar combination of Cu/S-Sn current collectors promotes stable SEI formation with better morphology retention even after Li plating/stripping for 10 cycles. After 10 cycles of operation, Li metal deposits were facilely removed from the Cu CC with shaking, indicating its firm contact with the CC, which enabled the cell to maintain a prolonged electrochemical stability (Figure 8k–m). Thus the cell assembled with a Li-rich manganese-based cathode (LMR)||Cu/C-Sn served as a stable interphase for guided Li deposition, lowered the voltage polarization, and maintained a C.E. of close to 99.4% after 20 cycles (Figure 8n,o) [69]. During continuous charge/discharge cycles, the SEI formation is also spontaneous resulting in the thickening of the interface, and provokes the development of dead Li which practically loses contact with the CC and causes short-circuiting. The block copolymeric coating (PFGM) produced by chemical induction on the Cu foil due to its extreme delocalization efficiency, reduces the Li-ion to its metallic counterpart, which during extended cycling conditions, allows the recovery of inaccessible Li metal and prevents accumulation at the SEI layer respectively. The cell with PFGM@Cu||NCM retains 54.8% of its capacity after 1000 cycles (Figure 8p), achieving a C.E. of 100% respectively [70]. Besides, the volume changes that occur in the cell during prolonged cycling were alleviated by in-situ fabricating electrospun copper nanofibre SEI layer (CuWs), which was effective in lowering the interfacial resistance, and promoting the uniform Li-ion distribution. Full cell combination of LFP||CuWs with a polyethylene (PE) separator cycled stably for around 30 cycles at 1C, with 92% capacity retention respectively [71]. Innovatively, Ouyang and his co-workers constructed a new programmable interphase layer using deoxyribonucleic acid (DNA) to facilitate the uniform distribution of Li^+ which eventually aids in enhanced reaction kinetics of Li, and when paired with LFP cathode, it exceptionally increased the C.E. to 186% than bare Cu CC. This strategy paves the way for the discovery of a new class of interphase materials that augments the stability of the fabricated anode-free batteries [72]. Similar works on the introduction of lithiophilic metals [73], and garnet electrolyte [74] on the Cu CC to form inorganic SEI can aid in the construction of stable interfacial chemistry which has a direct hand in assisting the development of highly stable ALLMBs.

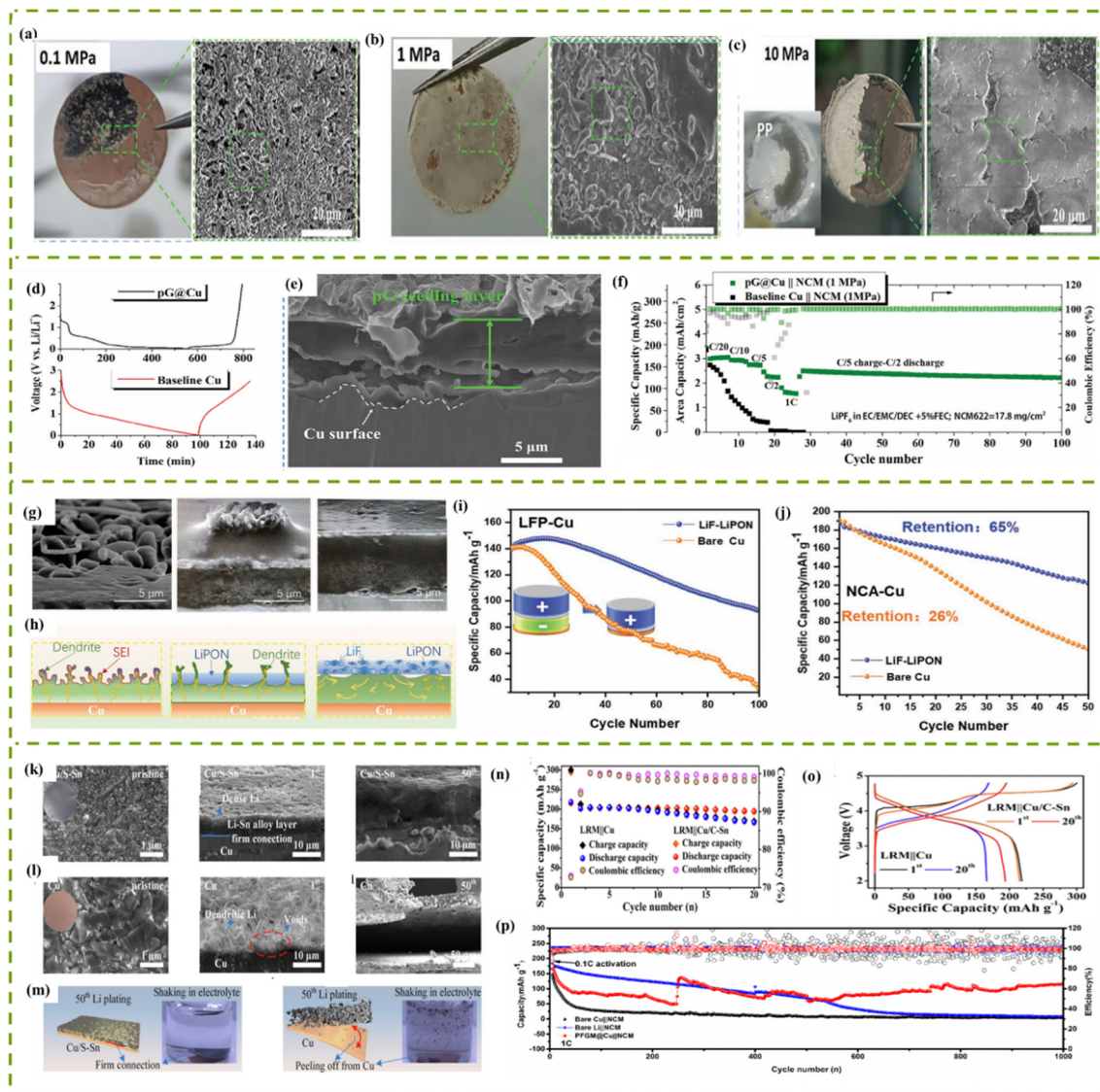


Figure 8. Digital images and SEM micrographs of plated Li morphologies on the Cu CC at (a) 0.1 MPa, (b) 1 MPa, and (c) 10 MPa, (d) Voltage curves, (e) SEM images of pG@Cu and Cu during initial lithiation, and (f) Cyclic performance of AF pG@Cu||NCM. Reproduced with permission from Ref. [66]. Copyright © 2023 Wiley-VCH GmbH, (g, h) SEM and schematic of Li deposition at pristine Cu, LiPON/Cu, and LiF-LiPON/Cu at 1 mAh cm⁻², Cyclic performance of (i) LFP with Cu and LiF-LiPON/Cu, and (j) NCA with Cu and LiF-LiPON/Cu. Reproduced with permission from Ref. [67]. Copyright © 2023 Wiley-VCH GmbH, (k, l) SEM images of Cu/S-Sn after Li plating at specified cycles, (m) Digital pictures of Li plating/stripping of Cu/S-Sn at 50th cycle, and (n, o) Electrochemical results of LRM||Cu/C-Sn. Reproduced with permission from Ref. [69]. Copyright © 2022 Elsevier B.V. Ltd., and (p) Cyclic performance of PFGM@Cu||NCM811. Reproduced with permission from Ref. [70]. Copyright © 2022 American Chemical Society.

3.2.2. Anode-Less Sodium Batteries

Correspondingly, the construction of an artificial mechanically robust sodium formate interface (HCOONa) would lower the electrolytic resistance and diffusion barrier and unveil the possibility of directed Na metal growth onto the anodic CC. It is been observed that the bare Na foils after gaseous treatment with HCOONa, exhibited a smooth morphology (Figure 9a) and when tested for their electrochemical efficiencies by charging and discharging at 2 mA cm⁻² and 1 mAh cm⁻², the symmetric HCOONa-Na||HCOONa-Na cell displayed ~45 mV of hysteresis voltage and was effective in extending the longevity (Figure 9b,c) of the cell structure [75]. Chemo-mechanical studies of Na plating/stripping behaviour concerning a deformable Li metal interface on the anodic Cu CC instead of using an Al CC were also studied using conductive carbon C45 as a nucleation layer. The pressure generated was averted uniformly due to the lowest elastic modulus of Li than Al and Cu CCs. This is evident in half-cell configuration Na||C45, where sodiation during the initial cycles reduced the irrevocable capacity loss, regulated a stable SEI erection, and helped in maintaining C.E. to around 99.8% (Figure 9d-f) for over 500 cycles [76].

Besides, erecting a carbon-aluminium interface to aggravate the sodium reversible behaviour has proved potent due to their ability to suppress Na dendrites, which thereby displayed an enlarged C.E. of 98.8% at 2 mA cm^{-2} , maintaining a stable performance for around 200 operational cycles (Figure 9g,h). Their corresponding plating/stripping morphology is depicted in Figure 9i,j [77]. Subsequently, the low lattice mismatch achieved between sodium-tin alloy (Na_9Sn_4) and the Al CC permitted homogeneous Na deposition at a high areal capacity by mitigating the lattice stress. This is because, the strong interaction of Sn with the electrolytic anions leads to the formation of an extremely thin SEI, which endows the cell with an areal capacity of 5 mAh cm^{-2} and a C.E. of 99.7% respectively. The Sn-Al||NVP cell exhibits 90 mAh g^{-1} of reversible capacity after 10 cycles and can light up LEDs connected in parallel [78]. This opens new horizons into the interrelationship between the alkaliphilic nature and lattice matching of the current collector, paving way for the formation of a stable inorganic SEI which is indispensable in augmenting the cycle life of ALSIB greatly.

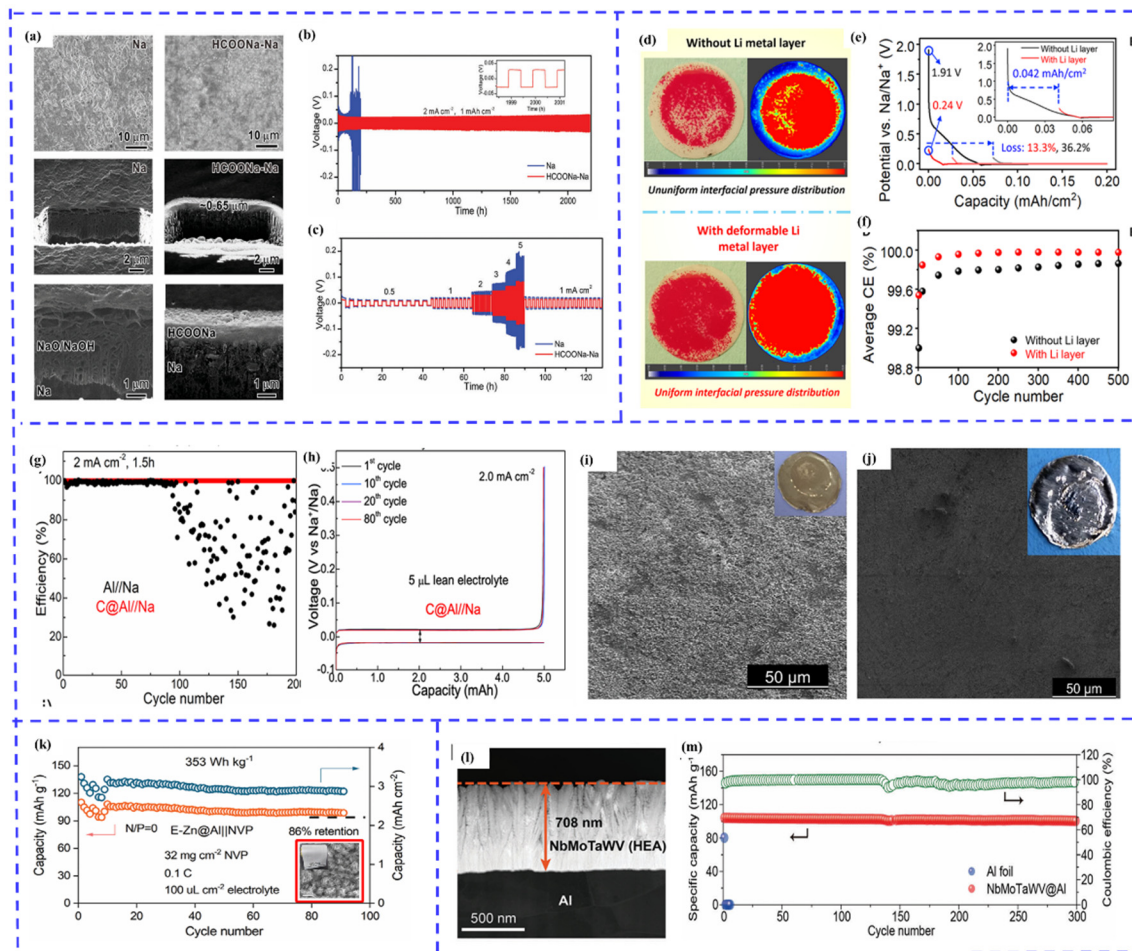


Figure 9. SEM and FIB micrographs of (a) Na and HCOONa-Na, Voltage curves of Na|Na and HCOONa-Na|HCOONa-Na at (b) 2 mA cm^{-2} , (c) $0.5\text{--}5 \text{ mA cm}^{-2}$. Reproduced with permission from Ref. [75]. Copyright © 2023 Wiley-VCH GmbH, (d) Pressure distribution on the NVP//C45 cell with and without Li layer, (e) Sodiation and the C45 layer plating/stripping at 0.04 mA cm^{-2} , and (f) C.E. at 0.5 mA cm^{-2} . Reproduced with permission from Ref. [76]. Copyright © 2024 Elsevier B.V., (g) Voltage curves of 1st cycle and C@Al/Na, (h) Profiles at $5 \mu\text{L}$ electrolyte conditions, SEM micrographs of (i) C@Al, and (j) Al CC after cycling for 50 cycles of plating and stripping at 3 mA cm^{-2} . Reproduced with permission from Ref. [77]. Copyright © 2023 American Chemical Society, (k) Cyclic performance of E-Zn@Al-Na||NVP cell at 0.1 C . Reproduced with permission from Ref. [80]. Copyright © 2024 Wiley-VCH GmbH, (l) HAADF image of the HEA-NbMoTaWV and its corresponding (m) Cyclic stability graphs. Reproduced with permission from Ref. [81]. Copyright © 2024 Wiley-VCH GmbH.

In highly anisotropic metals like zinc, a surface-regulated interface growth was promoted by plating/stripping Zn on a Bi substrate using a modulated solid-state surfactant approach, which lowers the nucleation overpotential and prevents the dendritic growth of Zn. The half-cell configuration with Zn|Bi cell uncovered a smooth surface devoid of Zn residues, capable of improving the cyclic stability for over 2400 h at a constant areal capacity of 5 mAh cm^{-2} respectively [79]. In recent years, high entropy materials have been widely employed to improve the

stability of SEI formed during cycling. In this context, the formation of a SEI layer with high entropy on the Al CC in the form of zinc, ordered with flower edges (E-Zn@Al-Na) exposing (100) and (101) facets donates electrons to promote interfacial decomposition, greater Na metal nucleation, and growth respectively. Meanwhile, the formed high-entropy SEI layer in AL E-Zn@Al-Na||NVP cell with a high-mass loaded cathode (32 mg cm^{-2}) facilitated better Na ion transfer retaining nearly 86% (Figure 9k) of its capacity after 90 cycles of operation [80]. Similarly, an interfacial layer with a high-entropy alloy composed of densely packed NbMoTaWV nanoplates was constructed on Al CC (NbMoTaWV@Al) to reduce the Na nucleation barrier and its corresponding over potential. The as-developed AF cell incorporating NbMoTaWV@Al at the anodic side achieved remarkable cyclic stability for over 300 cycles (Figure 9l,m) highlighting its unique properties to provide abundant sodiophilic sites which thereby improved the reaction kinetics of the cell greatly [81]. Thus, it is imperative to regulate the interfacial design with conformal thickness rationally, enabling better ionic transfer with emphasis on AM nucleation, pressure, and mechanical integrity.

3.3. Revamped Solvation in Electrolytes

Precise tuning of the electrolytic composition can have a noteworthy effect on the deposition morphology of Li and the nature of SEI layer formation. This is reflected during the decomposition of electrolytes that can even be channelized to form a desired SEI layer, which is vital in regulating the electrochemical behaviour of the cell favouring large ionic conductivity. Henceforth, modulating the additives and salt concentration in the liquid electrolyte can be effective in containing the AM ion inventory loss and can homogenize the Li flux during discharge cycles.

Anode-Less Metal Batteries

A cumulative additive 2,2,6,6-tetramethylpiperidine-1-oxyl (TEMPO) capable of redox shuttle was effectively integrated into the liquid electrolyte of AFLMBs by Zhang et al., where during charging, TEMPO oxidizes into its cationic counterpart and starts diffusing into the electrolyte. These TEMPO⁺ function as acceptors of electrons, oxidize the dead Li present in the electrolyte, and reactivate them into active Li ions. The voltage curves of AL-LMB with and without TEMPO⁺ are identical in their initial cycles, whereas the cell with TEMPO after 75 cycles showed minimal capacitive decay due to reduced polarization (Figure 10a–c), thereby influencing the C.E. of the battery [82]. During extended cycling, corrosion at the reactive metal anodes is obvious which instigates the formation of a cavity-like structure, exacerbating the Li dendrite formation, and aggravating safety concerns (Figure 10d–g). This was alleviated by replacing the solvent with 4M LiFSI in 1,2-dimethoxyethane (DME) instead of 1,2-dimethoxypropane (DMP), having poor solvation properties. Comparing their solvation properties, the deposition of Li was uniform and dense in DMP-based electrolytes than in DME. In AL Cu||NCM811 cell with 4M DMP, self-discharge is mitigated, thereby maintaining a stable C.E. for over 100 cycles and exhibiting only 0.03 V reduction in cut-off voltage (Figure 10h,i) [83].

In addition, the performance of different liquid electrolytes (LiTFSI, LiPF₆, and LiFSI) was contrasted using in situ polymerized electrolytes and Ga-based liquid metal at room temperature. The liquid metals play a major role by reducing the nucleation barrier required for Li deposition. The synergistic performance of GaInSn alloy in the 3M LiFSI electrolyte with DOL/DME solvent accedes the formation of a uniform Li-deposited morphology. The as-assembled ALB with optimized Li/LiFSI/NCM combination delivered an average C.E. of 99% (Figure 10j–k) and implicitly jeopardized the Li metal dendrite growth [84]. The longevity of the AL cells can be amplified by utilizing a dual carbonate-based electrolyte containing LiDFOB and LiBF₄, which when plated for different numbers of cycles and tested for its safety showed different plated morphologies and reactivities. Consecutively, the depletion of electrolytes at various pressure conditions was also analyzed, in which cells at higher pressure exhibited superior wetting capabilities accompanied by lower surface area and reduced porosity, vital for hindering the degradation [85]. Relatively, using a dual-salt electrolyte comprising LiDFOB and LiTFSI, with a mere amount of additive LiPF₆ added FEC and TTE solvent in a Cu||NMC cell showed different Li plating morphologies (Figure 10l–o) and exhibited 63% of capacity retention with 98.6% of C.E. after 50 cycles (Figure 10p) and the performance was 27% more when compared to the cell with an electrolyte containing single salt [86]. A similar configuration of electrolyte analyzing the effect of DEC solvent on 1 m LiDFOB and 0.05 m LiPF₆ in FEC, TTE, and DEC (Figure 10q,r) was investigated concerning their voltage and C.E.s [87].

Besides tuning the composition of salt, additives, and solvent in the electrolyte, preconcentrating 2M LiTFSI salt in 1-ethyl-3-methylimidazolium bis(trifluoromethylsulfonyl)imide on a nanoporous Al₂O₃ layer of Cu CC was effective in reducing the nucleation overpotential, activation energy, and enhancing the stability respectively. The as-fabricated AL cell with Al₂O₃-IL@Cu||NMC90 combination remarkably enhanced the rate performance and

stability of the cell [88]. Controlling the amount of sacrificial additives added to the electrolyte is equally important as they aid in the stable SEI layer formation. Jiang et al. fabricated an AL system with NCM811 cathode and assimilated LNO and diphenyl disulphide (DPDS) additives (SNA) into the DME solvent, where the cell retained 68.9% of its capacity after 50 cycles. It was also observed that the fracture of SEI is highly constrained due to the consistent release of SNA additives during extended cycling (Figure 11a–c), underscoring the significance of additive-enhanced electrolytes [89]. In addition to using dual salt concentrations in the electrolytes, incorporating trioxane (TO) in sulfolane (SF)/DME dual solvents with higher LiFSI concentration (DS-LHCE) promotes the formation of a stable LiF SEI layer on the Cu CC during cycling (Figure 11d). AL pouch cell Cu|| NMC811 configuration with DS-LHCE–1.3 + 0.15 TO electrolyte cycled stably for >200 cycles at room temperature with 80% capacity retention. The as-assembled ALB cell after undergoing hot formation (40 °C) at initial cycles, exhibited extraordinary safety performance when operated under a cell pressure of 1.2 MPa respectively [90].

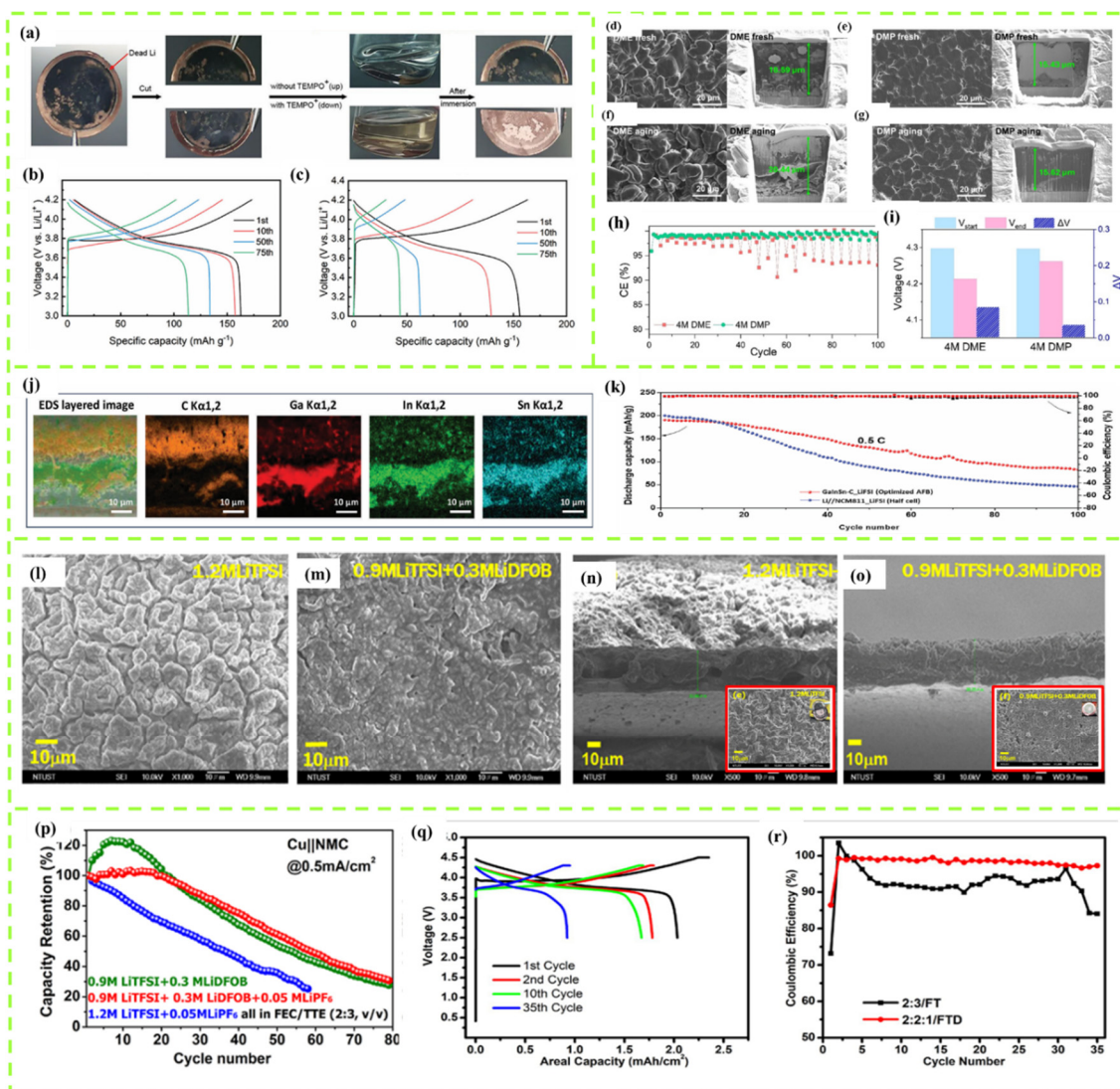


Figure 10. (a) Digital photographs of Li-plated Cu CC with and without the effect of TEMPO⁺, Charge/discharge curves of Cu||NMC AFLMB (b) with and (c) without TEMPO⁺. Reproduced with permission from Ref. [82]. Copyright © 2023 Wiley-VCH GmbH, (d–g) SEM images of deposited Li without and with rest in 4M DME and 4M DMP, (h) C.E. of cell with 4M DME and 4M DMP, (i) Voltage profiles of 4M DME and 4M DMP. Reproduced with permission from Ref. [83]. Copyright © 2024 Elsevier B.V., (j) EDAX images of CC@LM-C, and (k) Cycling performance of AF cells. Reproduced with permission from Ref. [84]. Copyright © 2024 Wiley-VCH GmbH, Top and cross-sectional SEM micrographs of cells cycled with Cu||NMC cell with (l, n) 1.2 M LiTFSI and (m, o) 0.9 M LiTFSI+0.3 M LiDFOB (inset shows the digital photograph of Cu CC discharged after 5th cycle), (p) Electrochemical performance of the Cu||NMC cell with different Li salts, Reproduced with permission from Ref. [86]. Copyright © 2022 Elsevier B.V., and (q, r) Charge/discharge profiles of Cu||NMC in FTD 2:2:1 and its corresponding C.E. Reproduced with permission from Ref. [87]. Copyright © 2020 Elsevier B.V.

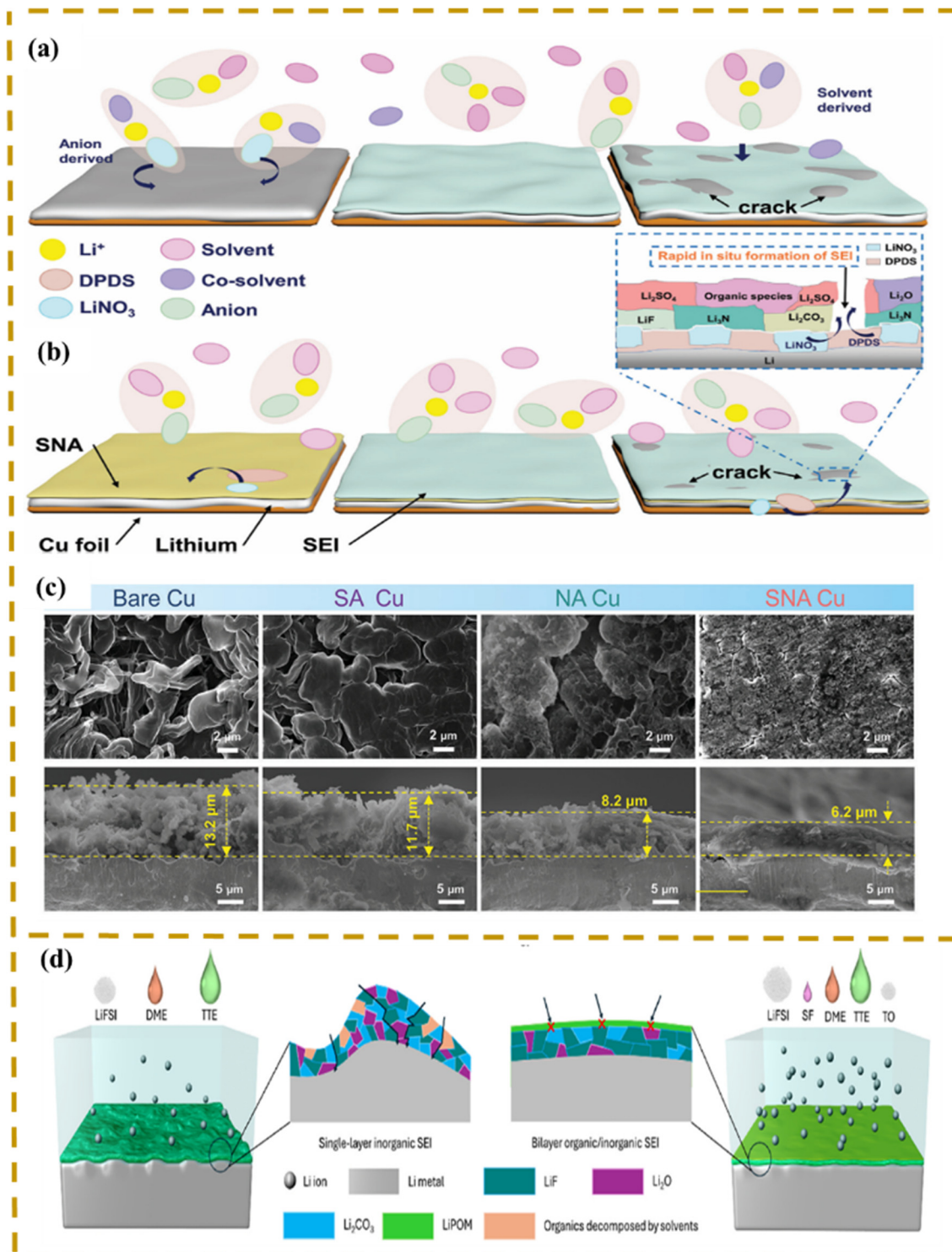


Figure 11. (a,b) Graphical representation of the influence of sacrificial LNO additive during cycling, (c) SEM micrographs of Li deposited CC surfaces, Reproduced with permission from Ref. [89]. Copyright © 2024 Wiley-VCH GmbH, and (d) Li deposition behaviour and the SEI layer formation in DME and DS-based LHCE solvents with TO. Reproduced with permission from Ref. [90]. Copyright © 2024 Elsevier Ltd.

Similarly, the effect of LNO additive in a reduced concentration of tetraethylene glycol dimethyl ether (TEGDME) electrolyte was studied, where the half-cell configuration 2M of LiTFSI improved the C.E. due to the stability conferred by the Li₂O to the SEI during cycling [91]. Contemporary research also focuses on developing post Li-ion metal batteries, because they can be used in aqueous environments without conceding their energy density [76,92]. In this aspect, aqueous zinc-based anode-free batteries have gained widespread interest owing to their lower redox potential and the cost-effectiveness of the zinc metal. However, the insufficient reversibility of Zn metal limits the longevity of the cell, which hinders their practical implementation. This was addressed by suitably regulating the nucleation and growth of zinc during the initial stages of cycling by Shi et al., where lithium

iodide was used as an additive in the electrolyte to significantly lower the nucleation overpotential. As a result, the Zn||iodine anode-free battery demonstrated exceptional cycling stability of over 10,000 cycles with nearly 88.2% of capacity retained at 0.99 mAh cm⁻² respectively [93].

The effect of Li deposition morphology on the Cu anode employing three different electrolytes such as dual-salt, conventional carbonate-based (LP57), and localized high-concentration electrolyte (LHCE) was investigated in AL-LMBs. Compared to the traditional LP57 electrolyte, Li morphology was even without nucleates with homogeneous distribution all over the Cu surface. Further, the electrochemical tests in the Li|Cu and Li|Li combinations uncovered the stable cycling performance with LHCE electrolyte having a consistent overpotential upsurge throughout charge/discharge [94]. The dual additive-enabled electrolyte also plays an eminent role in accelerating the mechanical stability and ionic conductivity of AL-LMBs. The synergy between ethylene sulphite (ES) and LiNO₃ in the 1M LiTFSI/DOL: DME electrolyte, enabled the formation of a stable SEI layer that maintains structural integrity, represses the dendritic growth of Li, and helps in achieving an appreciable electrochemical performance. The CC surface exhibited a smooth deposition morphology after the incorporation of the ES+LiNO₃ additive at varied current densities (Figure 12a–j) and the electrochemical performance of LFP||Cu-based AFBs with ES+LiNO₃ in LiTFSI electrolyte, retained 44.5% of its capacity and 99.2% of its C.E. after 100 cycles (Figure 12k,l) respectively [95].

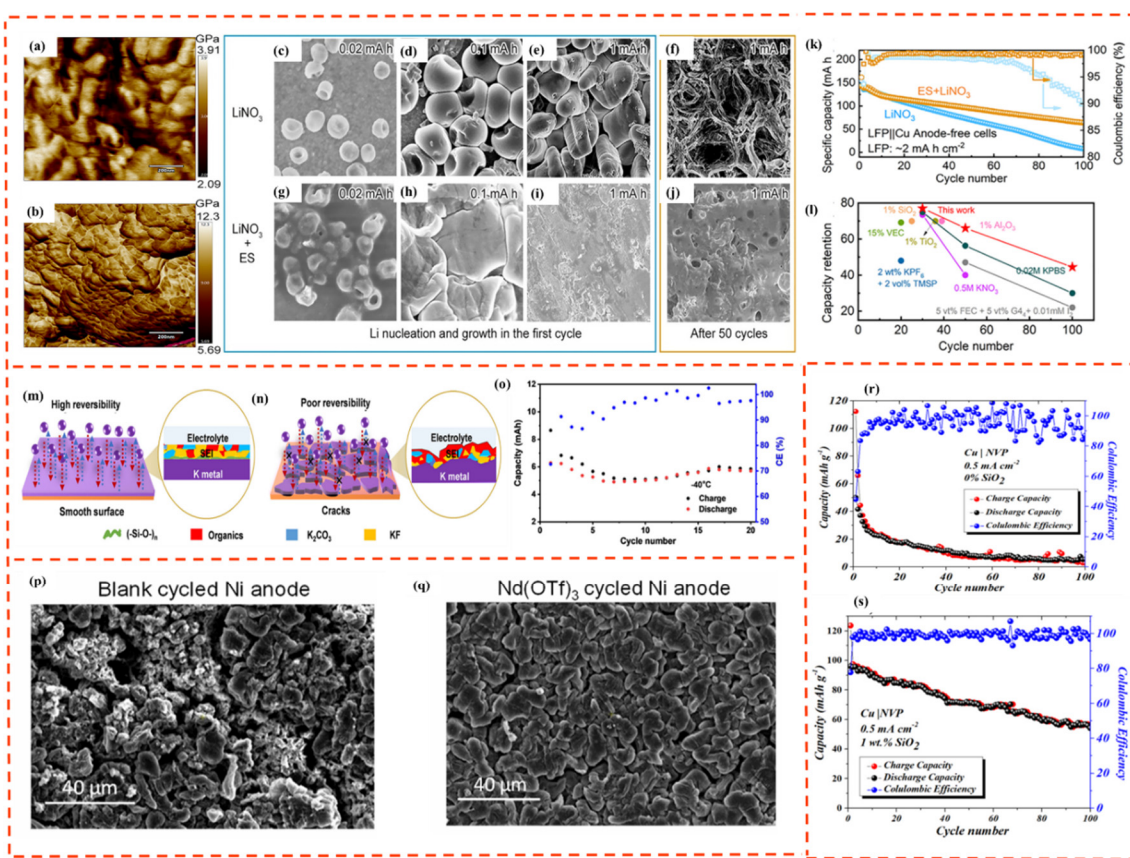


Figure 12. (a,b) Surface roughness of Li|Cu cell with LiNO₃ and ES+LiNO₃ additive enhanced cell, SEM micrographs of Li plating morphologies for cells comprising electrolyte with (c–j) LiNO₃ and ES+LiNO₃ additive at varied current densities, (k,l) Electrochemical results of AF LFP||Cu cell with ES+LiNO₃ additive, Reproduced with permission from Ref. [95]. Copyright © 2023 Press and Dalian Institute of Chemical Physics, Chinese Academy of Sciences. Published by ELSEVIER B.V. and Science Press, (m,n) Formation of SEI layer from 0.4 m KPF₆-DME electrolyte with and without PDMS additives, and (o) Specific capacities of the Cu||KPTCDA cell based on KPTCDA mass. Reproduced with permission from Ref. [96]. Copyright © 2023 Springer Ltd., (p,q) SEM micrographs of cycled Ni foil collected from Ni||Li₂S cell with plain and Nd(OTf)₃ enhanced electrolyte. Reproduced with permission from Ref. [97]. Copyright © 2024 American Chemical Society, (r,s) Cycling stability curves of Cu||NVP cells with conventional and SiO₂ additive enhanced electrolyte. Reproduced with permission from Ref. [98]. Copyright © 2024 Elsevier Ltd.

Moreover, realizing the use of anode-less AMBs at low temperatures is challenging as the formation of less-stable SEI layers together with aggravated dendrite formation is inevitable. Incorporating Si-O additives such as

polydimethylsiloxane (PDMS) into potassium hexafluorophosphate (KPF_6) in DME instigate the formation of an organic-inorganic hybrid Si-O-O and KF SEI layer, which proved potential for ameliorating the ionic reversibility and cyclability during K plating/stripping (Figure 12m–n). Assembly of the novel electrolyte with pre-potassiated 3,4,9,10-perylene tetracarboxylic acid-dianhydride||Cu (KPTCDA||Cu) exhibited a discharge capacity of 6.28 mAh g^{-1} during the initial cycles and retained nearly 90% of its capacity after 20 cycles of operation at -40°C (Figure 12o) [96]. An effective amalgamation of a neodymium triflate [$\text{Nd}(\text{OTf})_3$] additive into 1 m LiTFSI/DOL: DME electrolyte can inhibit the polysulphide shuttle, promote its adsorption, and implicitly stabilizes the Li plating/stripping behaviour. Li|| Li_2S cell with the prepared electrolyte combination exposes a compact and dense Li morphology (Figure 12p,q) at a C/10 rate after 20 cycles and aids in 78% capacity retention after 100 cycles [97].

Correspondingly, assimilating nano-silica as an additive into 1 m NaPF_6 in diglyme electrolyte facilitates better cationic Na transport and progressively induces stable nucleation-growth of Na onto the Cu CCs without dendrite agglomeration. The anode-less cell structure with Cu||NVP in conventional electrolyte without nano-silica displayed an unexpected drop in discharge capacity at 0.5 mA cm^{-2} , whereas the cell with 1 wt% nano-silica showed 75% capacity retention at 0.5 mA cm^{-2} after 50 cycles (Figure 12r,s) [98]. In addition, introducing hexamethyldisiloxane (HMDSO) additive into the electrolyte of AL cell with NVP cathode and GaInSn-coated Cu CC displayed 84.5 mAh g^{-1} of discharge capacity with 87.6% capacity retention, due to the synergistic effects of modified interfacial design and the additive enhanced electrolyte which was vital for improving the Na metal ion reversibility during extended cycling [99]. Another potential way to enhance the stability of the interface layer formed during cycling is to engineer the electrolyte solvation structure capable of operating at higher temperature conditions. So, an electrolyte design with an anion-stabilizing weak solvation structure was introduced to balance the interaction of Na^+ anion and Na^+ in the solvent. Benefitting from this structure, the multi-layered AL cell functioned stably for 50 cycles with 74.3% of capacity retained at -30°C , indicating enhanced reversibility of the Na during plating/stripping respectively [100].

Although the proposed strategies play a concurrent role in augmenting the rate capability, cyclic stability, and E.D. of the liquid electrolyte-based ALAMBs, the likelihood of accelerated short circuits due to dendrite growth can cause flammability of the conventionally used organic electrolytes leading to tragic cell failure. This calls for a paradigm shift toward solid-state electrolytes (SSE) which outperform conventional liquid electrolytes making it a promising alternative to realize higher E.D. without conceding safety.

4. Anode-Less Solid-State AMBs

The development of anode-less solid-state AMBs (AL-SSAMBs) is considered prominent due to the elimination of polymeric separators and the integration of SSEs that are devoid of the evolution of toxic gases, thermal runaway, and flammability as a consequence of battery short-circuiting. The intrinsic advantages of SSEs namely a wide electrochemical potential window, thermal and mechanical stability, and improved ionic conductivities at room temperature, makes them reliable for futuristic demands of high E.D. to drive the EV market in the world. However, their electrochemical performance is mainly constrained by the AM plating/stripping efficacy as there is deficient AM to replace the irrevocable loss, and the interplay between the electrode and SSE largely determines the C.E. and stability of the cell. In addition, the so-far-developed solid electrolytes' negated decomposition energy driven by the interfacial reactions at the anode exhibits thermodynamic instability against AM possessing reduced electrochemical potential. This majorly affects the electrochemical potential window of the SSEs. Further, the stability of the SSE is determined by the nature of the SEI formed, which jeopardizes the electrolytic ion reduction and affects the longevity of the cell during further cycling. Despite the presence of an enlarged reactive area at the interface between AM and SSE, the inhomogeneous AM deposition onto the CC influences the irreversible capacity loss. Henceforth, various cumulative efforts taken by the research community to appropriate a rationally designed CC and interface for an AL-SSAMB with a suitable solid electrolyte to heighten the cyclability are summarized as under.

Alkaliphilicity of the metallic CCs is a major concern in AL-SSAMBs as they are vital in validating the electrodeposition and electrodisolution kinetics that prompt dendrite growth. In this context, the attributes of an AL-SSLMB was analyzed using a sulfide-based SSE ($\text{Li}_6\text{PS}_5\text{Cl}$), with a telluride-coated Cu CC. The formed Li_2Te -alloy during extended charging/discharging significantly reduced the overpotential required for electrodeposition/electrodisolution with an overall improvement in C.E (Figure 13a–k). It is evidenced that Li_2Te forms a uniform wetting with stable deposition of Li. When assembled in an AL configuration of NMC|SE| Li_2Te -Cu, the cell exhibited stable cycling with 80% capacitive retention after 50 operational cycles [101]. In a similar study, the Cu CC surface was roughened to enhance the Li plating/stripping efficiency. The CC with a roughness

value of around 180 nm with a modulated sulfide solid electrolyte combination, augmented the reaction sites and reduced the SSE decomposition to increase the performance of AL-ASSBs [102]. To promote the solid-solution behaviour of Cu with SSE, atmospheric plasma spraying (APS) was implemented by Ockel et al. to endorse the adhesion of Cu CC with the solid electrolyte LAGP. This is facily promoted by considering the substrate temperature, particle velocity, thickness of coating, etc. It was found that a clear boundary was visible segregating both CC and the SE. In addition, the surface roughness is also higher on the surface after plasma spraying. Thus, the greater deposition rates achieved by APS render it more promising than conventional CVD/PVD techniques for large-scale commercialization of ALSSBs [103].

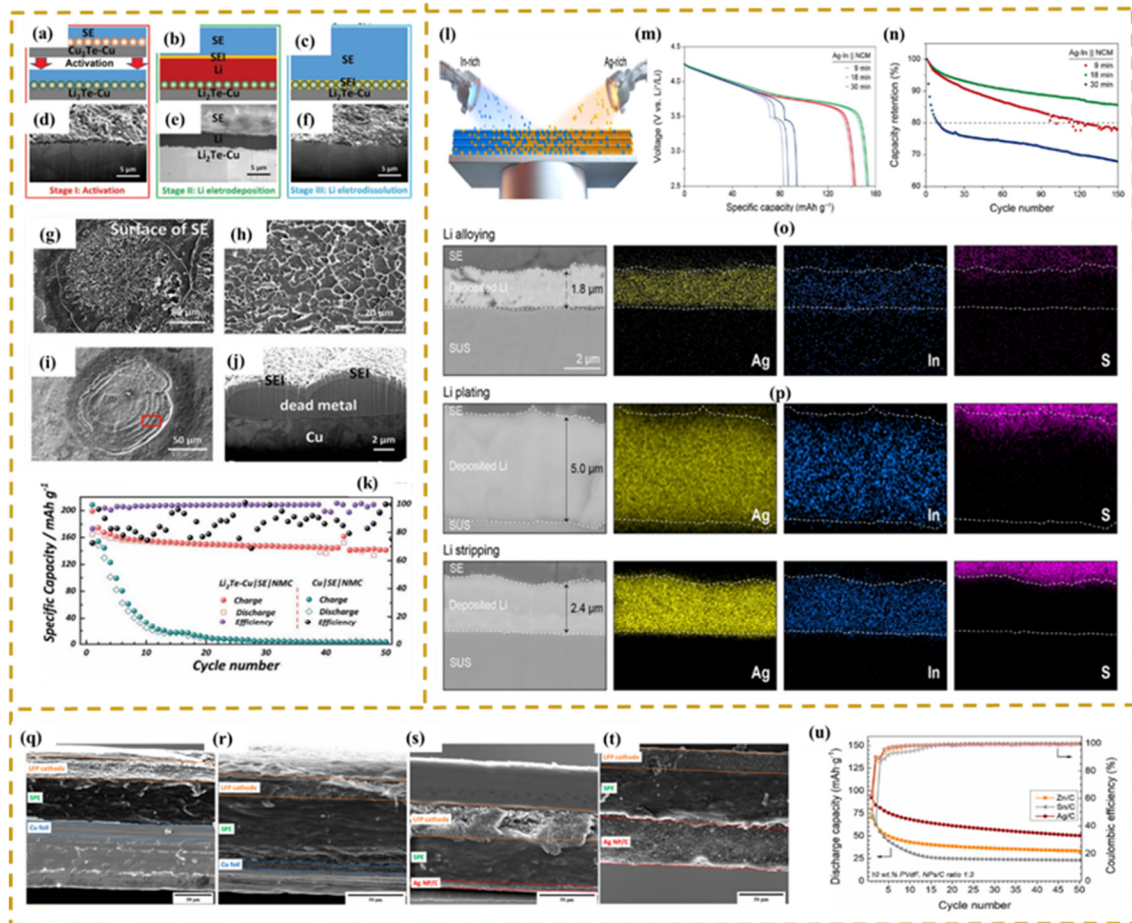


Figure 13. (a–c) Graphical representation and (d–f) SEM images of Li|SE|Li₂Te-Cu cell at three stages namely activation, electrodeposition (1 mAh cm⁻²), and electro-dissolution (1V), (g,h) SEM, (i,j) FIB images of the surface of SSE with SEI formation and dead metal accumulation, and (k) Cyclic performance of Li|SE|Li₂Te-Cu. Reproduced with permission from Ref. [101]. Copyright © 2022 Wiley-VCH GmbH, (l) Ag-In alloy metallic coating via CCS sputtering method, (m) Voltage profiles, (n) Retention curves of AL Ag-In|NMC cell, SEM and EDAX images of (o, p) Ag-In coated CCs during Li metal alloying, plating, and stripping. Reproduced with permission from Ref. [104]. Copyright © 2024 Elsevier B.V., (q–t) SEM micrographs of Ag NP/C enabled CC before and after charging, and (u) Discharge capacities of different metal nanocomposite coatings. Reproduced with permission from Ref. [105]. Copyright © 2022 Frontiers.

Lithiophilic coating on the CC with a multi-metal involving Ag and indium (In) via continuous composition spread sputtering (CCS) method was effective in the passivation of Li metal dendrite growth. Moreover, In owed to its inert nature can lower the SE decomposition behaviour (Figure 13l–n) and showed a homogeneous Li alloying and cycling morphology (Figure 13o,p). The Ag-In coated at different time intervals in the SUS CC, when paired with NCM cathode cycled stably between 4.3 and 2.4 V, and the one deposited at a lesser time interval delivered better performance improvement [104]. Further, the impact of different lithiophilic metals such as Sn, Zn, and Ag on the Cu CC was investigated, among which the Ag nanocomposite layer exhibited promising values of discharge capacity, retention capacity, and C.E. respectively. Also, the morphology of the cell with Ag NP/C|PEO-LiTFSI|LFP even after cycling showed minimal to null Li accumulation (Figure 13q–u) indicating the suitability of nanocomposite-based lithiophilic metal-coated CCs for use in ALAMBs [105]. A similar study by

Kim et al. validated the robustness of the Cu-Sn nanotube layer constructed onto the anodic layer to guide the Li deposition behaviour. After the initial stages of cycling, the Li_xSn phases in the Cu-Sn nanotube layers demonstrated better Li-ion diffusivity, which engendered the ALNCM with 99.85% of C.E. at room temperature with 83.8% capacity retention after 150 cycles of operation [106].

Curbing interfacial resistance has been an area of interest in improving ionic transfer as it provides pragmatic insights into Li deposition morphology. In this context, the failure mechanism behind introducing LLZTO SSE into ALLMBs was quantitatively analyzed. Though Au was sputtered onto the SSE to enhance the wettability property, the capacity loss was inherent at greater current densities due to lumped Li deposits on the surface of CC with traces of oxygen (Figure 14a,b). Moreover, the dendrite-shaped Li deposit displays a huge upper part indicating only a partial Li being stripped (Figure 14c). This was alleviated by the introduction of a PDMS elastomer to hinder pulverization, thus improving the electrochemical performance greatly. Half-cell measurements were vital for observing the short-circuit behaviour (Figure 14d,e) in cells without PDMS during cycling, whereas the cell with PDMS delivered a notable C.E. over the course of cycling [107]. Further, the influence of current density on the Li deposit nucleation on the Cu|LLZO interface was studied, and it was observed that ameliorating the current density facilitates heterogeneous deposition of Li (Figure 14f–i), highly anticipated for realizing a uniform coverage over the entire CC. However, this has to be leveraged by adopting thicker CCs or applying a uniform stack pressure [108]. Meanwhile, interfacial engineering using Li_2S as a promoter of an interfacial layer formation acts as a supplement for compensating the irreversible Li loss in the LFP cathode and when combined with a quasi-lean gel polymer electrolyte exhibited a specific capacity of 134 mAh g^{-1} after 100 cycles of operation with an average C.E. of 99.6% at 0.2C (Figure 14j,k). The increased enactment is due to the stable Li deposition behaviour without dendrite formation [109]. Similarly, the organization of the dual interface layer was effective in ion conduction and Li flux orientation. An anode-less solid-state configuration utilizing Ag-modified Cu CC with lithium polyacrylic acid-coated as the buffer layer (LiPAA-Ag/Cu)/ LiC_6 alongside LLZTO SSE/LCO cathode delivered 171.7 mAh g^{-1} of discharge capacity initially at 0.05 C (Figure 14l) with a retention of 80% after 20 operational cycles [110].

In another study, short-circuiting at lower current densities was avoided by erecting a nano-bilayer of tungsten (W) and magnesium (Mg) onto the anodic current collectors. The AL cell with NCM cathode, sulfide solid electrolyte, and W/Mg-Cu displayed a stable rate performance due to facile ion transport and compact dense morphology of the W/Mg layer during cycling [111]. Besides constructing a stable interlayer favorable for effective Li plating/stripping, adjustment of intrinsic pressure is equally essential to uphold firm contact between the SSE and the electrode. An AL cell with an NMC cathode, high ionically conductive sulfide SSE, and the anodic CC was erected by regulating the internal pressure with a compressible carbon felt placed between an SS rod and a CC (Figure 14m,n). The self-adjustable elastic layer increased the C.E. from 58.4% to 83.7%, followed by cycling stably for 100 operational cycles, achieving a critical current density of 1 mA cm^{-2} respectively [112]. During cell stacking, volume change accompanied by an intrinsic pressure build-up is unavoidable. This can be minimized by appropriately tailoring the anode structure with strain-free 3D titanium nitride (TiN) nanotubes in a vertical orientation. By embedding an Ag-C interlayer between the TiN nanotubes and LLZTO electrolyte, swift transport of Li metal is facilitated into the nanotube structure (Figure 14o), thereby promoting a homogeneous Li deposition [113]. Besides, to effectively mitigate the non-uniform Li metal deposition onto the anodic current collectors, Ma et al. devised anion-recognition electrodes, where the interactions of anion- π systems promoted better ion solvation in electrolytes accompanied by the formation of stable inner Helmholtz plane with a perpetual quadrupole moment (Q_{zz}) to enhance Li metal plating/stripping behaviour. In this context, among the various current collectors designed with differing Q_{zz} values, modified carbon cloth-based CC with greater Li metal plating/stripping behaviour achieved a C.E. of 99.1%, when tested for its efficiency in a carbonate-based electrolyte for over 230 cycles respectively [114]. In addition, to better comprehend the properties of Li metal electrodeposited onto the Cu CC during initial cycling, Becker et al. studied the microstructure of layers of Li deposited between the $\text{Li}_6\text{PS}_5\text{Cl}$ and steel interface. With reference to the Monte Carlo Potts model, it was concluded that the Li microstructure is independent of current density and is dependent on the layer thickness [115]. Furthermore, limited Na metal utilization due to poor interfacial contact between SSE and the Na metal anode enabled the introduction of a Pb/C interlayer to endorse the wettability to 0° at nearly 120° C . Moreover, the CCD for the half-cell with Na metal and NZSP SSE remained the same at all temperatures (Figure 14p) making them reliable for developing pragmatic AL-SSLMBs [116].

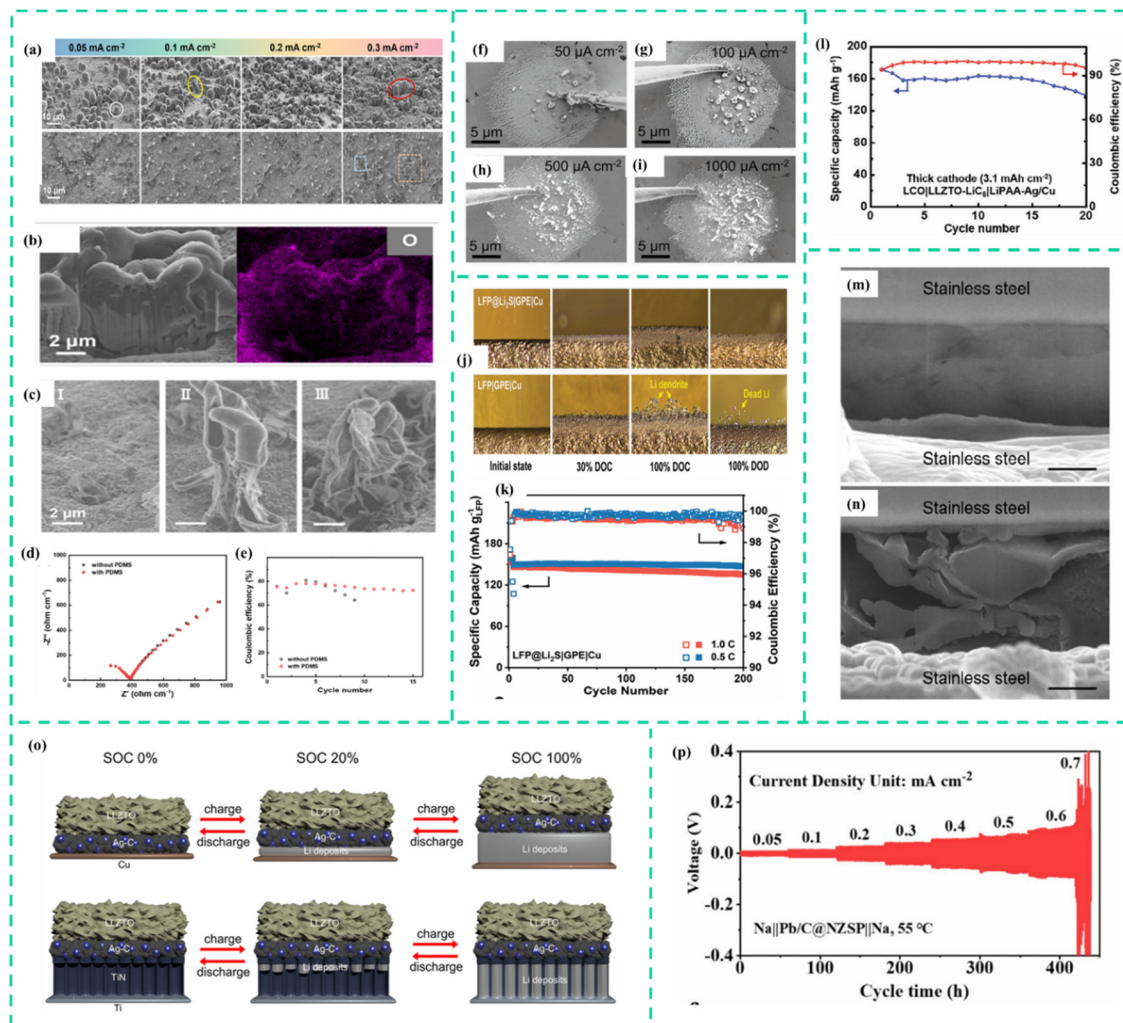


Figure 14. (a) Li plated morphologies at varied current densities, (b) Lump-shaped Li cross-section and its EDAX with the presence of O element, (c) Different Li morphologies after stripping, (d) Impedance, and (e) Stability graphs of Li|LLZTO|Au cells with and without the effect of PDMS membrane. Reproduced with permission from Ref. [107]. Copyright © 2022 Frontiers, (f–i) SEM images of Li-plated morphologies, Reproduced with permission from Ref. [108]. Copyright © 2022 The Authors. Advanced Energy Materials published by Wiley-VCH GmbH, (j) Li deposition morphologies on Cu CC surface, and (k) Cyclic performance of AL LFP@Li₂S|GPE|Cu and LFP|GPE|Cu. Reproduced with permission from Ref. [109]. Copyright © 2023 Wiley-VCH GmbH, (l) Cyclic stability of LFP|LLZTO-LiC₆|LiPAA-Ag/Cu. Reproduced with permission from Ref. [110]. Copyright © 2023 Wiley-VCH GmbH, (m,n) Effect of carbon-felt on the SS CC. Reproduced with permission from Ref. [112]. Copyright © 2023 American Chemical Society, (o) Pictorial representation of TiN NT- infiltrated LLZTO AL cell configuration. Reproduced with permission from Ref. [113]. Copyright © 2024 Springer Ltd., (p) Cyclic performance of Na||Pb/C@NZSP||Na at 55 °C. Reproduced with permission from Ref. [116]. Copyright © 2022 The Royal Society of Chemistry.

Despite the advantages posed by SSE in hindering flammability, and volatility, and providing enhanced thermal stability, their commercialization is impractical due to their constrained ionic conductivity and inferior interfacial properties. This was addressed by developing an intermediary quasi-SSE (QSE) with improved gelation behaviour to promote better ionic transport. However, the liquid component in QSE is prone to fire due to the presence of hydrocarbon-based solvents and plasticizers. So, hexafluorobutyl acrylate (HFBA) as a thermally stable monomer and pentaerythritol tetraacrylate (PETEA) as a cross-linker was used in a liquid electrolyte to convert into a QSE. At higher temperatures, the prepared HFBA-PETEA-based QSE can efficiently capture H radicals which causes combustion during cycling (Figure 15a). The Au/rGO||QSE||Li₂S-based AL cell exhibited 690.1 mAh g⁻¹ of discharge capacity initially and retained nearly 315.7 mAh g⁻¹ of specific capacity after 300 operational cycles (Figure 15b,c) displaying a stable performance [117]. Meanwhile, the elimination of an interlayer and pressure can provide realistic insights into the plating/stripping behaviour of Li in a sulfide-based AL-SSB. In this respect, halide and sulfide-based electrolytes with various chlorine concentrations were analyzed

for their electrochemical efficiencies. It was found that Li-argyrodites with the highest chlorine content namely $\text{Li}_{5.5}\text{PS}_{4.5}\text{Cl}_{1.5}$ outperformed other sulfide and halide combinations, and proved effective but faced a deterioration in C.E. in the initial cycles. This was mitigated by introducing an Ag-C interlayer due to the facile solid solution behaviour of Ag with Li and was able to improve the initial C.E. loss without any external stack pressure [118]. Correspondingly, a combination of $\text{Cu}|\text{CGPE}|\text{Li}_2\text{S}@\text{MX}$ displayed a dendrite-free smooth morphology at 1.2 mA cm^{-2} , whereas an origin of granular growth was evident in cells with liquid electrolyte, paving the way for mossy Li dendritic growth (Figure 15d). Further, a 0.51 Ah level capacity pouch cell with the CGPE configuration was able to deliver 340 Wh kg^{-1} of E.D. and could sustain continuous rolling and bending with a stable power output (Figure 15e,f) [119]. Active Li loss was further limited by fabricating an SSE comprising LiFSI and CsClO_4 and was compared with in situ polymerized LiPF_6 electrolyte. Li plating/stripping behaviour was enormously improved with $\text{LiFSI} + \text{CsClO}_4$ electrolyte, by obtaining a 3D porous morphology with a nominal Li deposition thickness, whereas with LiPF_6 the amount of porosity was close to 55% which may lead to irreversible loss of Li metal (Figure 15g–i). Also, it is found that the stable SEI layer formed during cycling (Figure 15j) lowers the capacitive loss of $\text{LiFSI} + \text{CsClO}_4$ electrolyte providing insights into the interrelationship between the Li deposition-dissolution and the AM reversibility during cycling [120]. Oxidative decomposition of the existing electrolytes in sodium batteries was suppressed by incorporating “liquid-in-solid” electrolytes with ether electrolytes in a liquid state effectually confined into the molecular sieves of zeolite (Na-SSZE). This improved the Na^+ transference number to 0.68 and when assembled in a 4.25 V AF pouch cell, it increased the cell E.D. to 412 Wh kg^{-1} and retained 89.2% of capacity retention after 370 cycles of operation [121]. Consequently, dendrite formation and the transition metal-ion dissolution from the cathodes of anode-free aqueous zinc batteries due to the side reaction induced by H_2O was combated by introducing a solid polymer electrolyte with poly(3 methacryloxypropyl trimethoxysilane) (PMPTS). This led to the formation of a structurally stable zinc-salt-rich inorganic hydrophobic SEI layer which was thermodynamically stable and achieved a very low overpotential of 126.1 mV at 10 mA cm^{-2} after 7000 hrs of cycling in a symmetric cell configuration. The anode-free configuration with the as-erected SPE retained nearly 99.2% of its capacity after 110 cycles respectively [122].

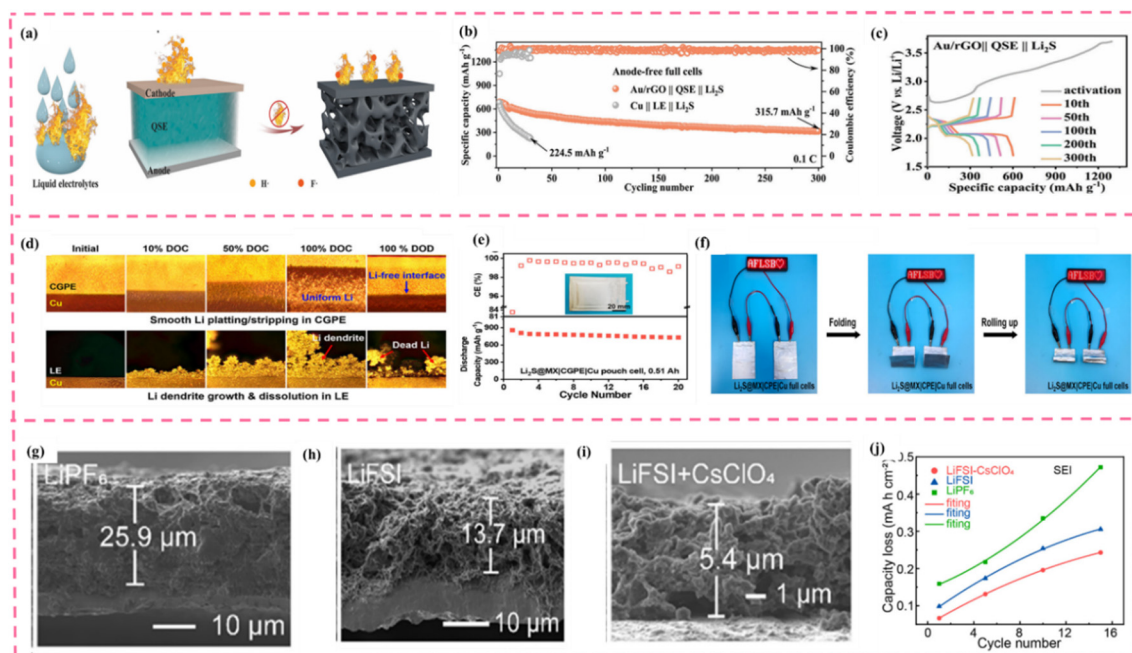


Figure 15. (a) Schematic of the advantage of QSE, and (b,c) Cyclic performance and specific capacity curves of AL $\text{Au/rGO}|\text{Li}_2\text{S}$ and $\text{Cu}|\text{Li}_2\text{S}$. Reproduced with permission from Ref. [117]. Copyright © 2023 Wiley-VCH GmbH, (d) Inoperando studies on Li deposition in $\text{Li}_2\text{S}@\text{MX}|\text{LE}|\text{Cu}$ and $\text{Li}_2\text{S}@\text{MX}|\text{CGPE}|\text{Cu}$, (e) Cyclic performance of $\text{Li}_2\text{S}@\text{MX}|\text{CGPE}|\text{Cu}$, and (f) LED powered by $\text{Li}_2\text{S}@\text{MX}|\text{CGPE}|\text{Cu}$ cells when connected in series. Reproduced with permission from Ref. [119]. Copyright © 2022 Springer Ltd., (g–i) SEM micrographs, and (j) Function of SEI vs. cycle number. Reproduced with permission from Ref. [120]. Copyright © 2024 Science Press and Dalian Institute of Chemical Physics, Chinese Academy of Sciences. Published by ELSEVIER B.V. and Science Press.

Although noteworthy strategies have been proposed to lessen the interfacial charge transfer resistance, the recovery of dead AM shows prominence as they are vital for enhancing the capacity and cyclic performance of

AL-SSAMBs. This requires careful selection of an SSE, which should be compatible and influence the ionic transport at room temperature. In addition, apart from using alkaliphilic metals for improving the wettability properties of the CC and the SSE, a tailored-made CC design to effectively relieve the stress and temperature generation during AL-SSAMB cycling also warrants further investigation. Besides, the role of cycling protocols has proved effective for upholding the AM inventory in the cell as the AM formation during the formation cycles plays a major role in the development of a stable SEI layer before cycling. Optimized cycling protocols investigating AM plating/stripping with modification in current densities, cycling conditions, temperature-dependent deposition, cut-off voltages, pressure, and salt concentration in electrolytes [123–127] cannot be undermined as their integration into the existing systems can provoke high-end commercialization in the future. Furthermore, upcoming research should necessarily focus on developing metal anodes with strain-relieved architectures by careful engineering of the CC or the electrodes in conventional, aqueous, and dual-ion batteries and should largely be studied using advanced characterization techniques to better interpret their interfacial and ion-transporting characteristics [128–132]. **Table 1** summarizes the electrochemical behaviour of all the anode-less alkali metal combinations discussed in this literature.

Table 1. Electrochemical performance of all the anode-less combinations discussed in this manuscript.

S. No.	Anode	Cathode	Electrolyte	Coulombic Efficiency	Capacity Retention	Stability	Ref.
1.	Cu-CNT	LiFePO ₄	1M LiTFSI in DME/DOL (1:1 v/v) + 3 wt% LiNO ₃	>95 %	69.4% at 0.5 C	100 cycles	[31]
2.	BPEI-Ag/LiNO ₃	NCM 811	1.3 M LiPF ₆ in EC/DEC (3:7 v/v) + 10 wt.% FEC	99%	52% at 4.2 mAh cm ⁻²	100 cycles	[32]
3.	Zn@NC@RGO@Cu	LiFePO ₄	1M LiTFSI in DME/DOL (1:1 v/v)	99.51%	61.4% at 0.6 C/1 C	100 cycles	[33]
4.	SiO ₂ @G-/Cu	LiFePO ₄	1M LiTFSI in DME/DOL (1:1 v/v) + 2 wt% LiNO ₃	98.62%	85.40% at 0.5 C	100 cycles	[36]
5.	Zn-N-CNF	LiFePO ₄	1M LiTFSI in DME	~100%	91% at 0.5 C	120 cycles	[37]
6.	Cu ₄₀ @Cu ₃ P	LiFePO ₄	1M LiTFSI in DME/DOL (1:1 v/v) + 2 wt% LiNO ₃	98.64%	-	-	[38]
7.	Cu-CNF-CNT	LiFePO ₄	1M LiTFSI in DME/DOL (1:1 v/v) + 2 wt% LiNO ₃	~100%	57.6%	100 cycles	[39]
8.	3D CC-MnO ₂	NCM532	0.6 mol LiDFOB+LiBF ₄ in FEC/DEC (1:2 v/v)	-	91% at 0.5 C	200 cycles	[40]
9.	Au/rGO	LiFePO ₄	1M LiTFSI in DME/DOL (1:1 v/v) + 2 wt% LiNO ₃	-	96% at 30 mA g ⁻¹	100 cycles	[41]
10.	HBSA-Co SA	NCM 811	1 M LiPF ₆ EC/DEC/DMC (1:1:1 v/v) + 1 wt% LiNO ₃	-	98.8% at 0.1 C	150 cycles	[42]
11.	HEA/CF	NCM 811	1 mol L ⁻¹ LiPF ₆ (v/v = 1:1:1 FEC 10%)	99.2%	71.8% at 1 C	160 cycles	[43]
12.	BCCC	NCM 811	EC/DEC (1:1 v/v)	99.1%	50% at 0.2 C	100 cycles	[44]
13.	Cu@β-PVDF	NCM	1 M LiPF ₆ in EC/DEC (1:1 v/v)	99.04%	61.45% at 0.2 mA cm ⁻²	30 cycles	[45]
14.	LDP @Cu-Ag	LiFePO ₄	1 M LiPF ₆ in EC/DEC/EMC (1:1:1 v/v/v) + 5 wt% FEC and 1M LiTFSI in DME/DOL (1:1 v/v) + 2 wt% LiNO ₃	-	-	-	[46]
15.	E-Cu	NCM811	6 M LiFSI in DME	~99%	84%	50 cycles	[47]
16.	LiF@PVDF/Cu	LiFePO ₄	1M LiTFSI in DME/DOL (1:1 v/v) + 3 wt% LiNO ₃	~99%	>20% at 1 C	-	[48]
17.	PI@Au	LiFePO ₄	1M LiTFSI in DME/DOL (1:1 v/v) + 2 wt% LiNO ₃	98.7%	20% at 0.5 mA cm ⁻²	340 cycles	[49]
18.	Cu@Si-PAN	LNMO	4.5 M FSI-TFSI	~99%	80%	120 cycles	[50]
19.	Cu-Mg	LiFePO ₄	1 M LiPF ₆ EC/DEC (1:1 v/v)	~70%	-	70 cycles	[51]
20.	Al@G	K-FeS ₂	4M KFSI in DME	>90%	>25%	30 cycles	[54]
21.	Cu-OSe NWs	K _{0.5} MnO ₂	4M KFSI in DME	>90%	63.5%	200 cycles	[55]
22.	Cu ₆ Sn@Cu	PTCDA	4M KFSI in DME	~100%	69.4% at 20 mA g ⁻¹	30 cycles	[56]
23.	Pb-Al@C	NVP	-	-	81.9%	200 cycles	[57]
24.	Na-MgF ₂ @NCHNF	NVP	1 M NaPF ₆ in diglyme	-	96% at 2 C	400 cycles	[58]
25.	Bi-NA@Cu	NTP	1 M NaPF ₆ in diglyme	~100%	93.22% at 1 C	267 cycles	[59]
26.	Al-Cu@C	NVP/C	1 M NaPF ₆ in diglyme	99.9%	>95% at 5 C	1300 cycles	[60]
27.	3D Zn@Al	NVP	1 M NaPF ₆ in DME	~100%	98.8% at 0.5 C	100 cycles	[61]
28.	Cu	NCM811@Li ₂ O	1 M LiTFSI + 1.5 M LiFSI in glycol dimethyl ether + HFE additive	~99%	80%	300 cycles	[65]
29.	pG@Cu	NMC622	1 LiPF ₆ in EC:DEC: EMC with 5% FEC	99.68%	89.5% at C/5 (charge)-C/2 (discharge)	100 cycles	[66]
30.	LiF-LiPON/Cu	LiFePO ₄	1M LiTFSI in DME/DOL (1:1 v/v) + 2 wt% LiNO ₃	-	66%	100 cycles	[67]
31.	Li ₄ Sn@Cu	NCM811	6M LiTFSI in DME	99%	85.5%	50 cycles	[68]

32.	Cu/C-Sn	LMR	1 LiPF ₆ in FEC:FEMC:HFE (2:6:2 wt%)	99.4%	>90%	20 cycles	[69]
33.	PFGM@Cu	NCM	1 LiPF ₆ in EC:DEC:EMC: (1:1:1 v/v) with 5% FEC	100%	54.8%	1000 cycles	[70]
34.	CuWs	LiFePO ₄	1M LiTFSI in DME/DOL (1:1 v/v) + 2 wt% LiNO ₃	>75%	92% at 1 C	30 cycles	[71]
35.	DNA-Cu	LiFePO ₄	1M LiTFSI in DME/DOL (4:1 v/v) + 3 wt% LiNO ₃	>95%	54.5%	400 cycles	[72]
36.	Cu	NVP	1 M NaPF ₆ in diglyme	~99%	88.2% at 0.5 C	400 cycles	[75]
37.	C-45@C	NVP	1 M NaPF ₆ in diglyme	99.97%	97.4% at C/3	100 cycles	[76]
38.	C@Al	NVP	1 M NaPF ₆ in diglyme	~100%	93%	100 cycles	[77]
39.	E-Zn@Al	NVP	1 M NaPF ₆ in diglyme	-	86% at 0.1 C	100 cycles	[80]
40.	NbMoTaWV@Al	NVP	1 M NaPF ₆ in DME	~99%	96.5%	300 cycles	[81]
41.	Cu	NCM	2M LiTFSI in DME/DOL (1:1 v/v) + 2 wt% LiNO ₃ + 1 wt% TEMPO additive	99.5%	71.8%	75 cycles	[82]
42.	Cu	NCM811	4 M LiFSI in DMP	~100%	-	-	[83]
43.	GaInSn-C	NCM811	3 M LiFSI in DOL/DME	99.7%	50% at 0.5 C	100 cycles	[84]
44.	Cu	NMC532	1.2 M LiPF ₆ in FEC:DEC and EC:DEC	-	-	200 cycles	[85]
45.	Cu	NCM	0.9M LiTFSI + 0.3M LiDFOB in FEC/TTE (2:3 v/v)	98.6%	63%	50 cycles	[86]
46.	Cu	NMC532	1 M LiDFOB + 0.05 M LiPF ₆ + FEC/TTE/DEC (2:2:1 v/v/v)	98.07%	45%	After 35th cycle	[87]
47.	Al ₂ O ₃ -IL@Cu	NMC90	2M LiTFSI in [EMIM][TFSI]	>80%	-	50 cycles	[88]
48.	SNA Cu	NCM811	DPDS and LNO in DME	>99%	68.9% at 0.3 C	60 cycles	[89]
49.	Cu	NCM811	DS-LHCE-1.3 + 0.15 TO	~100%	80%	206 cycles	[90]
50.	Cu	NMC111	0.6M LiDFOB + 0.6M LiBF ₄	~99%	-	100 cycles	[94]
51.	Cu	LiFePO ₄	1 M LiTFSI/DOL:DME + 2 wt% LiNO ₃	99.2%	44.5%	100 cycles	[95]
52.	Cu	KPTCDA	0.4M KPF ₆ DME with 2 vol.% PDMS	>98%	82% at 0.2 C	50 cycles	[96]
53.	Ni	Li ₂ S	1M LiTFSI+0.2M LiNO ₃ in DOL/DME (1:1 v/v) + 1.5 mM Nd(OTf) ₃	91%	62% at C/10 rate	60 cycles	[97]
54.	Cu	NVP	1 M NaPF ₆ in diglyme + 1 wt% SiO ₂	~99%	75%	100 cycles	[98]
55.	GaInSn-Cu	NVP	HMDSO in 1 M NaPF ₆ in diglyme	~99 %	87.6%	200 cycles	[99]
56.	Cu	NFM	2M NaPF ₆ in DEE	-	82.3% at 0.5 C	100 cycles	[100]
57.	Cu	NMC811	Li ₆ PS ₅ Cl	99%	80%	50 cycles	[101]
58.	Ag-In/Cu	NMC	Li ₆ PS ₅ Cl _{0.5} Br _{0.5}	99.8%	80.19% at 1 C	250 cycles	[104]
59.	Ag/C	LiFePO ₄	PEO-LiTFSI	-	-	-	[105]
60.	Cu-Sn NT	NCM811	Li ₆ PS ₅ Cl	99.85%	83.8%	150 cycles	[106]
61.	Au	LiFePO ₄	LLZTO	-	-	-	[107]
62.	Cu	LFP@Li ₂ S	GPE	~98.5%	65%	500 cycles	[109]
63.	Ag-Cu/LiPAA	LiFePO ₄	LiC ₆ -LLZTO	99.7%	90.3% at 0.1 C	120 cycles	[110]
64.	W/Mg	LiNbO ₃ -NMC811	Li ₆ PS ₅ Cl	99.7%	86.7%	200 cycles	[111]
65.	Ag-SUS	NMC	Li _{5.4} PS _{4.4} Cl _{1.6}	>99.5%	~55% at C/5	100 cycles	[112]
66.	Ag-C coated TiN NT	NMC	LLZTO	99.8%	78.3% at 60 °C	600 cycles	[113]
67.	CC-HPBF	NCM811	1 M LiPF ₆ in EC: EC:DEC	99.87%	-	200 cycles	[114]
68.	Na	NVP	Pb/C@NZSP	99.7%	96.5% at 0.5 C	200 cycles	[116]
69.	Au/rGO	Li ₂ S	HFBA-PETEA QSE	~99.99%	>40%	300 cycles	[117]
70.	Ag-C/SS	NMC811	Li _{5.5} PS _{4.5} Cl _{1.5}	99%	-	-	[118]
71.	Cu	Li ₂ S@MX	CGPE	~99%	60%	150 cycles	[119]
72.	Cu	Li	LiFSI + CsClO ₄	83.2%	-	-	[120]

5. Compensatory Effects in ALAMBs for Achieving Optimized Performance

Depletion of AM is caused by the SEI formation at the initial stages of cycling and the electrolytic degradation is recurrent during subsequent stages of cycling leading to the dead Li/Na/K formation. This however cannot be compensated by a renewed AM source, as all the AM in the system originates from the cathode. This rigorously limits the cyclability of the ALAMBs [133–136]. Henceforth, various approaches are being modulated to facilitate the perpetual recovery of the AM lost via cycling and other side reactions involving electrolytes and electrodes.

5.1. Modification of Cathode Material

One such strategy revolves around prelithiation/presodiation that can efficiently reduce the AM consumption during the formation of SEI, and these surplus AM sources can counterbalance the irreversible capacity loss. Two main approaches are proposed in this regard where (1) an appropriate amount of sacrificial AM salt addition namely Li₂S, Li₃N, Li₂O, etc. causes the metals to oxidize and generate gases such as CO₂, N₂, or CO which

indirectly affects the E.D. and (2) prelithiation/presodiation can serve as an AM reservoir, where the vacancies created in the crystal can accommodate more number of AM ions during first charge [137]. In a study by Lin and his group, Li-rich $\text{Li}_2[\text{Ni}_{0.8}\text{Co}_{0.1}\text{Mn}_{0.1}]\text{O}_2$ when used as a cathode for AL-LMB without the introduction of sacrificial agents endowed the cell with greater reversibility of Li-ions and delivered an enlarged E.D. of 447 Wh kg^{-1} respectively [138]. A similar configuration of Co-free spinel with Li-rich $\text{Li}_2\text{Ni}_{0.5}\text{Mn}_{1.5}\text{O}_4$ cathode cycled stably and delivered a large number of Li-ions at the initial charging process and in an AL configuration exhibited 367 Wh kg^{-1} of E.D. with 80% of capacity retained after 50 operational cycles [139]. A recent study by Xu et al. contrasted the effect of chemical and electrochemical prelithiation on NCM622 and NCM811 cathodes for anode-free Li metal batteries. It was observed that the electrochemically lithiated NCM622 cathode exhibited higher degree of lithiation eliminating the generation of by-products, and was found to cycle stably to >150 cycles with 80% of capacity retention when assembled in a coin cell [140]. Though prelithiation has proven adequate for a prolonged lifespan of the ALAMBs, structural changes encountered during cycling greatly results in significant capacitive decay. Tian et al. addressed this by fabricating a hybrid cathode consisting of NCM811 and LMO in the ratio of 3:1. Here, the greatly mass-loaded hybrid cathode with a balanced ratio of LMO and lean electrolyte conditions enhanced the as-assembled pouch cell's E.D. to 405 Wh kg^{-1} providing new perspectives into the concept of pre-lithiation [141]. Meanwhile, in SMBs, as $\text{Na}_3\text{V}_2(\text{PO}_4)_3$ can release only 2 Na ions/ Na_3VP , Wu et al. designed a Na-rich NASICON-type cathode, which during cycling transitions from Na_3VP to Na_4VP and then Na_5VP , delivering more Na ions to the system. The AL configuration retained 92% of its capacity at 1C displaying 320 Wh kg^{-1} of E.D. respectively [142]. Though these strategies were found operational, functional use of additive-enhanced electrolytes with prelithiated/presodiated cathodes can essentially prolong the life cycle and E.D. of ALAMBs.

5.2. Activation of Dead Li/Na/K

Dissolution of dendrites during extended cycling of ALAMBs leads to pulverization of the surface layer of the AM-plated CC, which results in the realization of dead Li/Na/K leading to the depletion of alkali metal sources. Dendrites usually do not consist of a pure alkali metal. They are mainly composed of an alloyed Li-compound such as the Li-carbide with a hollow and hard morphology that can easily penetrate the diaphragm causing battery short-circuits [143]. Most of the research studies focus on inhibiting dendritic growth to reduce dead alkali metal accumulation [144–146]. This was greatly addressed by introducing redox additives into the electrolyte capable of capturing the dead alkali metal and reactivating it. Calendar aging is one such phenomenon, where isolated AM recovery is accomplished at the discharge state to engender capacity enhancement, in addition to resting at the charged state to regulate the utilization of active AM in the electrolyte [147]. Thus, it is imperative to meticulously utilize an additive-enhanced electrolyte with an appropriate cycling protocol to improve dead AM recovery.

6. Conclusions and Future Outlook

Performance improvement in contemporarily used battery systems is constrained due to their increased demand for practical realization. Owing to their facile manufacturing process, structural optimization, and enlarged EDs, the ALAMB development is encouraging. However, the research enhancements carried out in this nascent field of study face commercial impediments due to inhomogeneous AM deposition, irreversible AM loss, and volume changes that halt further progress. This is because, the undiversified AM deposition at the interfaces tends to form dendrites, which eventually leads to stripping away of the dead AM at the top surface of dendrites during cycling. This depletes the active AM reservoir in the system and with subsequent cycles of deposition and stripping, there is a build-up of stress and volume changes in the cell increasing the chances of fracture of SEI aggravating side reactions with AM depletion. To address these challenges, effective appropriation strategies such as constructing alkaliphilic interfaces incorporating composite and alloyed 3D current collectors with protective coatings and modified interfacial layers can support competitive AM deposition by providing ample nucleation sites and balanced nucleation-growth rates, leading to uniform and dense deposition. Additionally, using dual and increased localized salt concentration in liquid and SSEs has been shown effectively to regulate ion transport and stabilize the SEI, thereby reducing the inherent stress and the side reactions. Meanwhile, the review also highlights the importance of post-Li metal batteries, with a few insights under each section on the emerging aqueous Zn batteries. Further, strategies to supplement AM, such as the use of supplementary AM additives, and AM-rich cathodes, can significantly replenish AM losses in the system. The importance of cycling protocols for both ALAMBs and ALSSAMBs has a direct impact on performance outcomes and has been effectually outlined in this article.

Even with the recent tremendous advancements, this field is still in the embryonic stage of development. To better comprehend the main scientific challenges and develop solutions for enhancing battery performance, more research is required. Herein, we provide several potential avenues for ALAMB development that could result in worthwhile and effective solutions as follows,

- (1) **Cyclic Stability:** Improvement in cyclic stability can be achieved by guided AM deposition. In addition to employing alkaliphilic CCs for reducing the nucleation overpotential during cycling, the design of 3D CCs with greater surface area is warranted, as it prevents coplanar growth of alkali metals resulting in more direction AM growth with stable interlayer formations. Apart from conventional techniques, novel and emergent methods like additive manufacturing (3D printing), and lithography can be effectively routed to fabricate 3D CCs with ease,
- (2) **Stable SEI Layer:** To alleviate the volume changes that the AM anodes experience during cycling, utilizing appropriate fluorine-based additives can appropriate the formation of a stable SEI layer with mechanical robustness, greater ionic conductivity, and can effectively hinder electrolytic degradation,
- (3) **Solid Polymer Electrolytes:** Promoting the use of alternative solid polymer composite electrolytes instead of widely experimented argyrodite-sulfide electrolytes for ALAMBs, can lessen the interfacial resistance and promote electrochemical stability of the system,
- (4) **Emergent Materials:** With a plethora of research on carbon-based coatings for regulating the metal deposition and conductivity of the electrodes/current collector, utilizing nanocarbon can be promising as it improves the alkaliphilic nature of the CC favouring uniform nucleation and growth of metal electrodeposition during cycling,
- (5) **Cycling Protocols:** Achieving greater ED and rate performance involves modifying the test conditions such as current density, stacking pressure, temperature, etc. However, cycling the cell at a reduced current density limits their practicality, and hence cycling protocols with optimized charge and discharge times can improve the stability and cycling,
- (6) **Other Parameters:** Moreover, the necessary construction of the metal anodes with stress-relief architectures and low tortuosity electrodes can effectively modulate the operating temperature, and the upper cut-off voltage range of the cell to help deliver greater EDs,
- (7) **Advanced Characterization Techniques:** Prospects on utilizing solid electrolytes for ALAMBs, require probing the solid solution behaviour, via advanced characterization techniques such as solid-state nuclear magnetic resonance (NMR), synchrotron X-ray, and neutron scattering for investigating their electronic structures, ionic movement, and predicting the position of AM in the solid structure,
- (8) **Dual-ion Batteries:** More research into dual-ion storage mechanisms instead of conventional “rocking chair” is highly warranted as it can necessarily compensate for the alkali-metal ion loss during cycling and can aid in improving both P.D. and E.D. simultaneously,
- (9) **Aqueous-based Systems:** High reactivity of the alkali metals engenders the development of aqueous batteries based on iron, zinc and aluminium, due to their cost-effectiveness, facile reversibility, safety, and comparable theoretical specific capacities as that of lithium,
- (10) **Deep Learning Models:** Since ALAMBs are still in their embryonic stage of development, integrating deep learning models into the existing battery production line is more challenging as it requires extensive databases on the properties and fundamental parameters of materials that define their electrochemical performance. However, the artificial intelligence-aided ALAMB design can address the challenges encountered during data collection for computing the typical interfacial formation, and can even provide insights into the material perspective, appropriate prediction on the microstructures, degradation mechanism, and can even quantify the AM inventory loss at the initial stages,
- (11) **Safety:** Safety is equally important as the influence of higher stacking pressure on the fabrication of Ah-class cells made from common SSEs including polymers, oxides, and sulfides requires safety testing with beneficial guidance.

Thus, the insights provided in this review offer an important research direction to realize practical ALAMBs to satisfy EVs’ energy and power density standards. In addition to moderating the current collector and interfaces, further research should necessarily focus on developing ALAMBs with greater mass-loaded cathodes, and thin electrolytes that facilitate the formation of a stable SEI layer endowing the cell with greater electrochemical performance. However, the fundamental limitation of achieving desirable cyclic stability as compared to conventional MIBs, can be effectually overcome by appropriate cell engineering that can achieve C.E. and stability up to 100% and >500 cycles respectively for enhancing the ionic reversibility and improving the characteristics of ALAMBs.

Author Contributions

S.K.: Writing—Original draft, Methodology, Conceptualization, Formal analysis, A.R.: Conceptualization, Supervision, Resources, Writing—Reviewing and Editing, Funding acquisition. All authors have read and agreed to the published version of the manuscript.

Funding

This research was financially supported by the Department of Science and Technology (DST), New Delhi, India, under a research grant of Storage MAP Scheme No. DST/TMD/IC-MAP/2K20/01, Indo-German Project Scheme no. DST/INT/DAAD/P-12/2022, AMEST Scheme No. DST/CEST/AMEST/2022/57 and UGC-DAE-CSR, Indore ref. no. CRS/2021-22/04/614.

Data Availability Statement

Not applicable.

Conflicts of Interest

The authors declare no conflict of interest.

References

1. Zor, C.; Turrell, S.J.; Uyanik, M.S.; et al. Lithium Plating and Stripping: Toward Anode-Free Solid-State Batteries. *Adv. Energy Sustain. Res.* **2024**, *5*, 2300001. <https://doi.org/10.1002/aesr.202300001>.
2. Zhao, C.; Xu, G.-L.; Yu, Z.; et al. A high-energy and long-cycling lithium–sulfur pouch cell via a macroporous catalytic cathode with double-end binding sites. *Nat. Nanotechnol.* **2021**, *16*, 166–173. <https://doi.org/10.1038/s41565-020-00797-w>.
3. Hagen, M.; Hanselmann, D.; Ahlbrecht, K.; et al. Lithium–Sulfur Cells: The Gap between the State-of-the-Art and the Requirements for High Energy Battery Cells. *Adv. Energy Mater.* **2015**, *5*, 1401986. <https://doi.org/10.1002/aenm.201401986>.
4. Chen, Y.; Ye, C.; Zhang, N.; et al. Prospects for practical anode-free sodium batteries. *Mater. Today* **2024**, *73*, 260–274. <https://doi.org/10.1016/j.mattod.2024.01.002>.
5. Manthiram, A. A reflection on lithium-ion battery cathode chemistry. *Nat. Commun.* **2020**, *11*, 1550. <https://doi.org/10.1038/s41467-020-15355-0>.
6. Chen, J.; Wang, Y.; Li, S.; et al. Porous Metal Current Collectors for Alkali Metal Batteries. *Adv. Sci.* **2023**, *10*, 2205695. <https://doi.org/10.1002/advs.202205695>.
7. Kim, S.; Park, G.; Lee, S.J.; et al. Lithium-Metal Batteries: From Fundamental Research to Industrialization. *Adv. Mater.* **2023**, *35*, 2206625. <https://doi.org/10.1002/adma.202206625>.
8. Zhang, Y.; Zhong, Y.; Wu, Z.; et al. Solvent Molecule Cooperation Enhancing Lithium Metal Battery Performance at Both Electrodes. *Angew. Chem. Int. Ed.* **2020**, *59*, 7797–7802. <https://doi.org/10.1002/anie.202000023>.
9. Fang, C.; Li, J.; Zhang, M.; et al. Quantifying inactive lithium in lithium metal batteries. *Nature* **2019**, *572*, 511–515. <https://doi.org/10.1038/s41586-019-1481-z>.
10. Chen, K.-H.; Wood, K.N.; Kazyak, E.; et al. Dead lithium: Mass transport effects on voltage, capacity, and failure of lithium metal anodes. *J. Mater. Chem. A* **2017**, *5*, 11671–11681. <https://doi.org/10.1039/C7TA00371D>.
11. Schmich, R.; Wagner, R.; Hörpel, G.; et al. Performance and cost of materials for lithium-based rechargeable automotive batteries. *Nat. Energy* **2018**, *3*, 267–278. <https://doi.org/10.1038/s41560-018-0107-2>.
12. Yim, C.-H.; Houache, M.S.E.; Baranova, E.A.; et al. Understanding key limiting factors for the development of all-solid-state-batteries. *Chem. Eng. J. Adv.* **2023**, *13*, 100436. <https://doi.org/10.1016/j.cej.2022.100436>.
13. Hatzell, K.B. Anode-Less or Anode-Free? *ACS Energy Lett.* **2023**, *8*, 4775–4776. <https://doi.org/10.1021/acsenergylett.3c02163>.
14. Neudecker, B.J.; Dudney, N.J.; Bates, J.B. “Lithium-Free” Thin-Film Battery with In Situ Plated Li Anode. *J. Electrochem. Soc.* **2000**, *147*, 517. <https://doi.org/10.1149/1.1393226>.
15. Nanda, S.; Gupta, A.; Manthiram, A. Anode-Free Full Cells: A Pathway to High-Energy Density Lithium-Metal Batteries. *Adv. Energy Mater.* **2021**, *11*, 2000804. <https://doi.org/10.1002/aenm.202000804>.
16. Wu, W.; Luo, W.; Huang, Y. Less is more: A perspective on thinning lithium metal towards high-energy-density rechargeable lithium batteries. *Chem. Soc. Rev.* **2023**, *52*, 2553–2572. <https://doi.org/10.1039/D2CS00606E>.
17. Yao, W.; Zou, P.; Wang, M.; et al. Design Principle, Optimization Strategies, and Future Perspectives of Anode-Free Configurations for High-Energy Rechargeable Metal Batteries. *Electrochem. Energy Rev.* **2021**, *4*, 601–631. <https://doi.org/10.1007/s41918-021-00106-6>.

18. Pei, A.; Zheng, G.; Shi, F.; et al. Nanoscale Nucleation and Growth of Electrodeposited Lithium Metal. *Nano Lett.* **2017**, *17*, 1132–1139. <https://doi.org/10.1021/acs.nanolett.6b04755>.
19. Huo, S.; Wang, L.; Su, B.; et al. Anode-Free Li Metal Batteries: Feasibility Analysis and Practical Strategy. *Adv. Mater.* **2024**, *36*, 2411757. <https://doi.org/10.1002/adma.202411757>.
20. Lai, T.; Zhao, H.; Song, Y.; et al. Mechanism and Control Strategies of Lithium-Ion Battery Safety: A Review. *Small Methods* **2024**, *9*, 2400029. <https://doi.org/10.1002/smt.202400029>.
21. Betz, J.; Bieker, G.; Meister, P.; et al. Theoretical versus Practical Energy: A Plea for More Transparency in the Energy Calculation of Different Rechargeable Battery Systems. *Adv. Energy Mater.* **2019**, *9*, 1900761. <https://doi.org/10.1002/aenm.201900761>.
22. Wu, B.; Chen, C.; Rajmakers, L.H.J.; et al. Li-growth and SEI engineering for anode-free Li-metal rechargeable batteries: A review of current advances. *Energy Storage Mater.* **2023**, *57*, 508–539. <https://doi.org/10.1016/j.ensm.2023.02.036>.
23. Heubner, C.; Maletti, S.; Auer, H.; et al. From Lithium-Metal toward Anode-Free Solid-State Batteries: Current Developments, Issues, and Challenges. *Adv. Funct. Mater.* **2021**, *31*, 2106608. <https://doi.org/10.1002/adfm.202106608>.
24. Tudela Ribes, A.; Beaunier, P.; Willmann, P.; et al. Correlation between cycling efficiency and surface morphology of electrodeposited lithium. Effect of fluorinated surface active additives. *J. Power Sources* **1996**, *58*, 189–195. [https://doi.org/10.1016/S0378-7753\(96\)02397-X](https://doi.org/10.1016/S0378-7753(96)02397-X).
25. Zhang, X.-Q.; Wang, X.-M.; Li, B.-Q.; et al. Crosstalk shielding of transition metal ions for long cycling lithium–metal batteries. *J. Mater. Chem. A* **2020**, *8*, 4283–4289. <https://doi.org/10.1039/C9TA12269A>.
26. Cooper, E.R.; Li, M.; Gentle, I.; et al. A Deeper Understanding of Metal Nucleation and Growth in Rechargeable Metal Batteries Through Theory and Experiment. *Angew. Chem. Int. Ed.* **2023**, *62*, e202309247. <https://doi.org/10.1002/anie.202309247>.
27. Xu, H.; Li, S.; Chen, X.; et al. Surpassing lithium metal rechargeable batteries with self-supporting Li–Sn–Sb foil anode. *Nano Energy* **2020**, *74*, 104815. <https://doi.org/10.1016/j.nanoen.2020.104815>.
28. Lu, Y.; Zhao, C.-Z.; Zhang, R.; et al. The carrier transition from Li atoms to Li vacancies in solid-state lithium alloy anodes. *Sci. Adv.* **2021**, *7*, eabi5520. <https://doi.org/10.1126/sciadv.abi5520>.
29. Song, H.; He, T.; Liu, J.; et al. Conformal coating of lithium-zinc alloy on 3D conducting scaffold for high areal capacity dendrite-free lithium metal batteries. *Carbon* **2021**, *181*, 99–106. <https://doi.org/10.1016/j.carbon.2021.05.002>.
30. Hong, S.-H.; Jung, D.-H.; Kim, J.-H.; et al. Electrical Conductivity Gradient Based on Heterofibrous Scaffolds for Stable Lithium-Metal Batteries. *Adv. Funct. Mater.* **2020**, *30*, 1908868. <https://doi.org/10.1002/adfm.201908868>.
31. Shan, C.; Qin, Z.; Xie, Y.; et al. Cu-CNTs current collector fabricated by deformation-driven metallurgy for anode-free Li metal batteries. *Carbon* **2023**, *204*, 367–376. <https://doi.org/10.1016/j.carbon.2022.12.074>.
32. Cho, S.; Kim, D.Y.; Lee, J.-I.; et al. Highly Reversible Lithium Host Materials for High-Energy-Density Anode-Free Lithium Metal Batteries. *Adv. Funct. Mater.* **2022**, *32*, 2208629. <https://doi.org/10.1002/adfm.202208629>.
33. Huang, S.; Lu, S.; Lv, Y.; et al. Single-atomic Zn-(C/N/O) lithiophilic sites induced stable lithium plating/stripping in anode-free lithium metal battery. *Nano Res.* **2023**, *16*, 11473–11485. <https://doi.org/10.1007/s12274-023-5795-7>.
34. Abdollahifar, M. Nanocarbon applications in anode-free batteries. *Carbon* **2025**, *233*, 119914. <https://doi.org/10.1016/j.carbon.2024.119914>.
35. Gu, J.; Zhang, Y.; Shi, Y.; et al. Heteroatom Immobilization Engineering toward High-Performance Metal Anodes. *ACS Nano* **2024**, *18*, 25966–25985. <https://doi.org/10.1021/acs.nano.4c08831>.
36. Ding, S.; Fang, Z.; Zhang, L.; et al. Organic nano carbon source inducing 3D silica nanoparticles-graphene nanosheet layer on Cu current collector for high-performance anode-free lithium metal batteries. *J. Colloid Interface Sci.* **2024**, *672*, 543–551. <https://doi.org/10.1016/j.jcis.2024.06.043>.
37. Zhang, X.-L.; Ma, L.; Cai, Y.-P.; et al. A low-Fermi-level current collector enables anode-free lithium metal batteries with long cycle life. *Matter* **2024**, *7*, 583–602. <https://doi.org/10.1016/j.matt.2023.11.017>.
38. You, X.; Feng, Y.; Ning, D.; et al. Phosphorized 3D Current Collector for High-Energy Anode-Free Lithium Metal Batteries. *Nano Lett.* **2024**, *24*, 11367–11375. <https://doi.org/10.1021/acs.nanolett.4c01844>.
39. Zhong, G.; Ma, J.; Li, N.; et al. Ultralight, dual-conductive, all-fiber based 3D anode current collector for anode-free lithium metal battery. *Carbon* **2024**, *228*, 119424. <https://doi.org/10.1016/j.carbon.2024.119424>.
40. Deng, J.; Li, H.; Zheng, F.; et al. A “breathable” 3D lithium host with MnO₂ nanoflake array for long-lifespan anode-free lithium metal batteries. *Chin. Chem. Lett.* **2024**, 110681. <https://doi.org/10.1016/j.ccl.2024.110681>.
41. Li, J.; Ma, Z.; Yang, K.; et al. Laser-Generated Au nanoparticles as lithophilic sites in self-supported film host for anode-free lithium metal battery. *J. Colloid Interface Sci.* **2025**, *678*, 578–587. <https://doi.org/10.1016/j.jcis.2024.09.049>.
42. Zhu, J.; Kang, C.; Xiao, X.; et al. Regulating local chemical softness of the collector to homogenize Li deposition for anode-free Li-metal batteries. *Energy Environ. Sci.* **2024**, *17*, 9323–9334. <https://doi.org/10.1039/D4EE03673E>.

43. Wang, J.; Yang, P.; Wang, Y.; et al. High entropy alloy nanoparticles decorated carbon-based electrode as interfacial Li-ion localized accelerators for anode-free lithium metal batteries. *Carbon* **2024**, *228*, 119432. <https://doi.org/10.1016/j.carbon.2024.119432>.
44. Liao, X.; Wang, X.; Yan, C.; et al. Bipolar Current Collectors of Cu/polymer/Al Composite for Anode-Free Batteries. *Adv. Funct. Mater.* **2024**, *34*, 2310925. <https://doi.org/10.1002/adfm.202310925>.
45. Abrha, L.H.; Nikodimos, Y.; Weldeyohannes, H.H.; et al. Effects of a Thermally Electrochemically Activated β -PVDF Fiber on Suppression of Li Dendrite Growth for Anode-Free Batteries. *ACS Appl. Energy Mater.* **2021**, *4*, 3240–3248. <https://doi.org/10.1021/acsaem.0c03015>.
46. Yang, B.; Wei, H.; Wang, H.; et al. Engineering Moderately Lithiophilic Paper-Based Current Collectors with Variable Solid Electrolyte Interface Films for Anode-Free Lithium Batteries. *Nanomaterials* **2024**, *14*, 1461. <https://doi.org/10.3390/nano14171461>.
47. Lin, L.; Suo, L.; Hu, Y.-S.; et al. Epitaxial Induced Plating Current-Collector Lasting Lifespan of Anode-Free Lithium Metal Battery. *Adv. Energy Mater.* **2021**, *11*, 2003709. <https://doi.org/10.1002/aenm.202003709>.
48. Tamwattana, O.; Park, H.; Kim, J.; et al. High-Dielectric Polymer Coating for Uniform Lithium Deposition in Anode-Free Lithium Batteries. *ACS Energy Lett.* **2021**, *6*, 4416–4425. <https://doi.org/10.1021/acsaenergylett.1c02224>.
49. Weldeyohannes, H.H.; Abrha, L.H.; Nikodimos, Y.; et al. Guiding lithium-ion flux to avoid cell's short circuit and extend cycle life for an anode-free lithium metal battery. *J. Power Sources* **2021**, *506*, 230204. <https://doi.org/10.1016/j.jpowsour.2021.230204>.
50. Liang, P.; Sun, H.; Huang, C.-L.; et al. A Nonflammable High-Voltage 4.7 V Anode-Free Lithium Battery. *Adv. Mater.* **2022**, *34*, 2207361. <https://doi.org/10.1002/adma.202207361>.
51. Nan, W.; Li, B.; Yan, S.; et al. Dynamic interface layer enables epitaxial Li deposition for anode-free Li metal batteries. *J. Phys. Chem. Solids* **2025**, *196*, 112350. <https://doi.org/10.1016/j.jpcs.2024.112350>.
52. Zhang, W.; Zhang, F.; Ming, F.; et al. Sodium-ion battery anodes: Status and future trends. *EnergyChem* **2019**, *1*, 100012. <https://doi.org/10.1016/j.enchem.2019.100012>.
53. Kim, D.-Y.; Kim, D.-H.; Kim, S.-H.; et al. Nano Hard Carbon Anodes for Sodium-Ion Batteries. *Nanomaterials* **2019**, *9*, 793. <https://doi.org/10.3390/nano9050793>.
54. Zhao, Y.; Liu, B.; Yi, Y.; et al. An Anode-Free Potassium-Metal Battery Enabled by a Directly Grown Graphene-Modulated Aluminum Current Collector. *Adv. Mater.* **2022**, *34*, 2202902. <https://doi.org/10.1002/adma.202202902>.
55. Cui, Z.; Song, J.; Chen, M.; et al. Non-completely selenized Cu-OSe nanowires as potassium-philic host for anode-free potassium metal batteries. *Energy Storage Mater.* **2024**, *71*, 103649. <https://doi.org/10.1016/j.ensm.2024.103649>.
56. Ren, N.; Wang, L.; Li, X.; et al. Design Principles of Mediation Layer for Current Collectors Toward High-Performance Anode-Free Potassium-Metal Batteries: A Case Study of Cu₆Sn₅ on Copper. *Adv. Funct. Mater.* **2024**, *34*, 2313538. <https://doi.org/10.1002/adfm.202313538>.
57. Wu, H.; Xie, C.; Zhang, M.; et al. Retarded sodium alloying interface reaction for stable anode-less sodium metal batteries. *Chem. Commun.* **2024**, *60*, 8264–8267. <https://doi.org/10.1039/D4CC02545H>.
58. Guo, W.; Liu, X.; Mu, Y.; et al. Outside-in directional sodium deposition through self-supporting gradient fluorinated magnesium alloy framework toward high-rate anode-free Na batteries. *Energy Storage Mater.* **2024**, *73*, 103840. <https://doi.org/10.1016/j.ensm.2024.103840>.
59. Bai, Y.; Zheng, X.; Liu, H.; et al. Honeycomb-like superstructure of 3D sodiophilic host for anode-free sodium batteries. *Energy Storage Mater.* **2025**, *74*, 103926. <https://doi.org/10.1016/j.ensm.2024.103926>.
60. Li, H.; Zhang, H.; Wu, F.; et al. Sodiophilic Current Collectors Based on MOF-Derived Nanocomposites for Anode-Less Na-Metal Batteries. *Adv. Energy Mater.* **2022**, *12*, 2202293. <https://doi.org/10.1002/aenm.202202293>.
61. Cai, Z.; Tang, F.; Yang, Y.; et al. A multifunctional super-sodiophilic coating on aluminum current collector for high-performance anode-free Na-metal batteries. *Nano Energy* **2023**, *116*, 108814. <https://doi.org/10.1016/j.nanoen.2023.108814>.
62. Xu, K.; Zheng, X.; Luo, R.; et al. A three-dimensional zincophilic nano-copper host enables dendrite-free and anode-free Zn batteries. *Mater. Today Energy* **2023**, *34*, 101284. <https://doi.org/10.1016/j.mtener.2023.101284>.
63. Pan, Y.; Liu, Z.; Liu, S.; et al. Quasi-Decoupled Solid-Liquid Hybrid Electrolyte for Highly Reversible Interfacial Reaction in Aqueous Zinc-Manganese Battery. *Adv. Energy Mater.* **2023**, *13*, 2203766. <https://doi.org/10.1002/aenm.202203766>.
64. Yan, C.; Xu, R.; Xiao, Y.; et al. Toward Critical Electrode/Electrolyte Interfaces in Rechargeable Batteries. *Adv. Funct. Mater.* **2020**, *30*, 1909887. <https://doi.org/10.1002/adfm.201909887>.
65. Qiao, Y.; Yang, H.; Chang, Z.; et al. A high-energy-density and long-life initial-anode-free lithium battery enabled by a Li₂O sacrificial agent. *Nat. Energy* **2021**, *6*, 653–662. <https://doi.org/10.1038/s41560-021-00839-0>.

66. Liu, W.; Luo, Y.; Hu, Y.; et al. Interrelation Between External Pressure, SEI Structure, and Electrodeposit Morphology in an Anode-Free Lithium Metal Battery. *Adv. Energy Mater.* **2024**, *14*, 2302261. <https://doi.org/10.1002/aenm.202302261>.
67. Sun, J.; Zhang, S.; Li, J.; et al. Robust Transport: An Artificial Solid Electrolyte Interphase Design for Anode-Free Lithium-Metal Batteries. *Adv. Mater.* **2023**, *35*, 2209404. <https://doi.org/10.1002/adma.202209404>.
68. Zhang, Z.; Luo, H.; Liu, Z.; et al. A chemical lithiation induced Li_{4.4}Sn lithiophilic layer for anode-free lithium metal batteries. *J. Mater. Chem. A* **2022**, *10*, 9670–9679. <https://doi.org/10.1039/D2TA00167E>.
69. Wang, X.; He, Y.; Tu, S.; Fu, L.; et al. Li plating on alloy with superior electro-mechanical stability for high energy density anode-free batteries. *Energy Storage Mater.* **2022**, *49*, 135–143.
70. Ma, C.; Weng, S.; Zhang, Y.; et al. Chemically Induced Activity Recovery of Isolated Lithium in Anode-free Lithium Metal Batteries. *Nano Lett.* **2022**, *22*, 9268–9274. <https://doi.org/10.1021/acs.nanolett.2c02508>.
71. Liu, X.; Liu, J.; Zhao, H.; et al. In-situ construction of high-performance artificial solid electrolyte interface layer on anode surfaces for anode-free lithium metal batteries. *J. Colloid Interface Sci.* **2025**, *679*, 1106–1116. <https://doi.org/10.1016/j.jcis.2024.10.023>.
72. Ouyang, Z.; Wang, Y.; Wang, S.; et al. Programmable DNA Interphase Layers for High-Performance Anode-Free Lithium Metal Batteries. *Adv. Mater.* **2024**, *36*, 2401114. <https://doi.org/10.1002/adma.202401114>.
73. Yu, K.; Chen, J.; xie, X.; et al. Constructing LiF-rich artificial SEI at a two-dimensional copper net current collector in anode-free lithium metal batteries. *Surf. Interfaces* **2022**, *34*, 102326. <https://doi.org/10.1016/j.surfin.2022.102326>.
74. Abrha, L.H.; Zegeye, T.A.; Hagos, T.T.; et al. Li₇La_{2.75}Ca_{0.25}Zr_{1.75}Nb_{0.25}O₁₂@LiClO₄ composite film derived solid electrolyte interphase for anode-free lithium metal battery. *Electrochim. Acta* **2019**, *325*, 134825. <https://doi.org/10.1016/j.electacta.2019.134825>.
75. Wang, C.; Zheng, Y.; Chen, Z.-N.; et al. Robust Anode-Free Sodium Metal Batteries Enabled by Artificial Sodium Formate Interface. *Adv. Energy Mater.* **2023**, *13*, 2204125. <https://doi.org/10.1002/aenm.202204125>.
76. Jiao, W.; Alaci, S.; Ramamurthy, J.; et al. Highly stable anode-free sodium batteries enabled by mechanically deformable nucleation interface. *Energy Storage Mater.* **2024**, *73*, 103784. <https://doi.org/10.1016/j.ensm.2024.103784>.
77. Dahunsi, O.J.; Li, B.; An, B.; et al. Directing High-Efficiency Na Plating with Carbon–Aluminum Junction Interfaces for Anode-Free Na Metal Batteries. *Energy Fuels* **2023**, *37*, 7522–7529. <https://doi.org/10.1021/acs.energyfuels.3c00891>.
78. Ma, P.; Zhang, Y.; Li, W.; et al. Tailoring alloy-reaction-induced semi-coherent interface to guide sodium nucleation and growth for long-term anode-less sodium-metal batteries. *Sci. China Mater.* **2024**, *67*, 3648–3657. <https://doi.org/10.1007/s40843-024-3084-4>.
79. Wang, C.; Chen, B.; Wang, T.; et al. Sustainable interface regulation enabled by a bismuth solid-state surfactant effect for Zn-free anodes. *Energy Environ. Sci.* **2024**, *17*, 5429–5439. <https://doi.org/10.1039/D4EE01644K>.
80. Ge, J.; Ma, C.; Zhang, Y.; et al. Edge Electron Effect Induced High-Entropy SEI for Durable Anode-Free Sodium Batteries. *Adv. Mater.* **2024**, 2413253. <https://doi.org/10.1002/adma.202413253>.
81. Liu, L.; Cai, Z.; Yang, S.; et al. Multifunctional High-Entropy Alloy Nanolayer Toward Long-Life Anode-Free Sodium Metal Battery. *Adv. Mater.* **2024**, *37*, 2413331. <https://doi.org/10.1002/adma.202413331>.
82. Zhang, Y.; Liu, J.; Li, Y.; et al. Reactivating the Dead Lithium by Redox Shuttle to Promote the Efficient Utilization of Lithium for Anode Free Lithium Metal Batteries. *Adv. Funct. Mater.* **2023**, *33*, 2301332. <https://doi.org/10.1002/adfm.202301332>.
83. Lee, J.; Kim, J.; Lee, D.G.; et al. Constructing stable solid electrolyte interphases to enhance the calendar life of anode-free lithium metal batteries. *Chem. Eng. J.* **2024**, *499*, 156296.
84. Nguyen, M.H.; Kim, D.; Kim, B.-K.; et al. Harnessing Liquid Metals with In Situ Polymerized Electrolyte for Anode-Free Lithium Metal Batteries. *Adv. Funct. Mater.* **2024**, *34*, 2407179. <https://doi.org/10.1002/adfm.202407179>.
85. Louli, A.J.; Eldesoky, A.; Weber, R.; et al. Diagnosing and correcting anode-free cell failure via electrolyte and morphological analysis. *Nat. Energy* **2020**, *5*, 693–702. <https://doi.org/10.1038/s41560-020-0668-8>.
86. Beyene, T.T.; Su, W.-N.; Hwang, B.J. Dilute dual-salt electrolyte for successful passivation of in-situ deposited Li anode and permit effective cycling of high voltage anode free batteries. *J. Power Sources* **2022**, *542*, 231752. <https://doi.org/10.1016/j.jpowsour.2022.231752>.
87. Jote, B.A.; Beyene, T.T.; Sahalie, N.A.; et al. Effect of diethyl carbonate solvent with fluorinated solvents as electrolyte system for anode free battery. *J. Power Sources* **2020**, *461*, 228102. <https://doi.org/10.1016/j.jpowsour.2020.228102>.
88. Anansuksawat, N.; Sangsanit, T.; Prempluem, S.; et al. Preconcentration of lithium salt in nanoporous alumina on Cu foil as a concentrated lithium semi-solid layer for anode-free Li-metal batteries. *Chem. Commun.* **2024**, *60*, 14380–14383. <https://doi.org/10.1039/d4cc03946g>.
89. Jiang, R.; Zhu, Z.; Qi, X.; et al. N, S-Rich SEI Derived From Continuously-Releasing Additive for Anode-Free Lithium-Metal Batteries in Commercial Carbonate Electrolyte. *Small* **2024**, 2410486. <https://doi.org/10.1002/smll.202410486>.

90. Qin, K.; Sasaki, T.; Ge, S.; et al. Enhanced salt content and stabilized bilayer passivation interphase toward long-life and high-safety anode-free lithium battery. *Mater. Today Energy* **2025**, *47*, 101751. <https://doi.org/10.1016/j.mtener.2024.101751>.
91. Wang, Y.; Noguchi, H. Revealing the enhancement of Li plating/stripping efficiency in TEGDME-based low-concentration electrolytes for anode-free lithium metal batteries. *Phys. Chem. Chem. Phys.* **2024**, *26*, 25352–25362. <https://doi.org/10.1039/D4CP02755H>.
92. Lu, C.; Zhao, F.; Tao, B.; et al. Anode-Free Aqueous Aluminum Ion Batteries. *Small* **2024**, *20*, 2402025. <https://doi.org/10.1002/sml.202402025>.
93. Shi, W.; Song, Z.; Zhang, W.; et al. Identifying iodide-ion regulation of early-stage zinc nucleation and growth for high-rate anode-free zinc metal batteries. *Energy Environ. Sci.* **2024**, *17*, 7372–7381. <https://doi.org/10.1039/D4EE02784A>.
94. Su, L.; Charalambous, H.; Cui, Z.; et al. High-efficiency, anode-free lithium–metal batteries with a close-packed homogeneous lithium morphology. *Energy Environ. Sci.* **2022**, *15*, 843–854. <https://doi.org/10.1039/D1EE03103A>.
95. Lin, Y.; Chen, J.; Zhang, H.; et al. In-situ construction of high-mechanical-strength and fast-ion-conductivity interphase for anode-free Li battery. *J. Energy Chem.* **2023**, *80*, 207–214. <https://doi.org/10.1016/j.jechem.2023.02.005>.
96. Tang, M.; Dong, S.; Wang, J.; et al. Low-temperature anode-free potassium metal batteries. *Nat. Commun.* **2023**, *14*, 6006. <https://doi.org/10.1038/s41467-023-41778-6>.
97. Yen, Y.-J.; Manthiram, A. Anode-Free Lithium–Sulfur Batteries with a Rare-Earth Triflate as a Dual-Function Electrolyte Additive. *ACS Appl. Mater. Interfaces* **2024**, *16*, 34997–35005. <https://doi.org/10.1021/acsmi.4c05414>.
98. Panchal, R.A.; Datta, J.; Varude, V.; et al. Nano-silica electrolyte additive enables dendrite suppression in an anode-free sodium metal battery. *Nano Energy* **2024**, *129*, 110010. <https://doi.org/10.1016/j.nanoen.2024.110010>.
99. Ji, H.; Xie, C.; Zhang, R.; et al. Sodiophilic Interface and Electrolyte Regulation Boost the Lifespan of Anode-Free Sodium Battery. *SusMat* **2024**, e258. <https://doi.org/10.1002/sus2.258>.
100. Zou, Y.; Zhang, B.; Luo, H.; et al. Electrolyte Solvation Engineering Stabilizing Anode-Free Sodium Metal Battery With 4.0 V-Class Layered Oxide Cathode. *Adv. Mater.* **2024**, *36*, 2410261. <https://doi.org/10.1002/adma.202410261>.
101. Wang, Y.; Liu, Y.; Nguyen, M.; et al. Stable Anode-Free All-Solid-State Lithium Battery through Tuned Metal Wetting on the Copper Current Collector. *Adv. Mater.* **2023**, *35*, 2206762. <https://doi.org/10.1002/adma.202206762>.
102. Gu, D.; Kim, H.; Lee, J.-H.; et al. Surface-roughened current collectors for anode-free all-solid-state batteries. *J. Energy Chem.* **2022**, *70*, 248–257. <https://doi.org/10.1016/j.jechem.2022.02.034>.
103. Ockel, M.; Borchers, A.; Fröhlich, J.; et al. Atmospheric Plasma Spraying for Copper Coating of Ceramic Solid Electrolytes for Anode-Free Solid-State Batteries with Increased Interfacial Contact. In Proceedings of the 2024 1st International Conference on Production Technologies and Systems for E-Mobility (EPTS), Bamberg, Germany, 5–6 June 2024; pp. 1–5.
104. Lee, J.H.; Oh, S.-H.; Yim, H.; et al. Interfacial stabilization strategy via In-doped Ag metal coating enables a high cycle life of anode-free solid-state Li batteries. *Energy Storage Mater.* **2024**, *69*, 103398. <https://doi.org/10.1016/j.ensm.2024.103398>.
105. Garcia-Calvo, O.; Gutiérrez-Pardo, A.; Combarro, I.; et al. Selection and Surface Modifications of Current Collectors for Anode-Free Polymer-Based Solid-State Batteries. *Front. Chem.* **2022**, *10*, 934365. <https://doi.org/10.3389/fchem.2022.934365>.
106. Kim, J.; Lee, S.; Kim, J.; et al. Regulating Li electrodeposition by constructing Cu–Sn nanotube thin layer for reliable and robust anode-free all-solid-state batteries. *Carbon Energy* **2024**, *6*, e610. <https://doi.org/10.1002/cey2.610>.
107. Zhang, Y.; Hu, X.; Peng, X.; et al. Electrochemical sintering of lithium metal constrained by buffer layer in anode-free all-solid-state batteries. *Energy Storage Mater.* **2024**, *72*, 103762. <https://doi.org/10.1016/j.ensm.2024.103762>.
108. Fuchs, T.; Becker, J.; Haslam, C.G.; et al. Current-Dependent Lithium Metal Growth Modes in “Anode-Free” Solid-State Batteries at the Cu|LLZO Interface. *Adv. Energy Mater.* **2023**, *13*, 2203174. <https://doi.org/10.1002/aenm.202203174>.
109. Liu, Y.; Meng, X.; Shi, Y.; et al. Long-Life Quasi-Solid-State Anode-Free Batteries Enabled by Li Compensation Coupled Interface Engineering. *Adv. Mater.* **2023**, *35*, 2305386. <https://doi.org/10.1002/adma.202305386>.
110. Wen, J.; Wang, T.; Wang, C.; et al. A Tailored Interface Design for Anode-Free Solid-State Batteries. *Adv. Mater.* **2024**, *36*, 2307732. <https://doi.org/10.1002/adma.202307732>.
111. Oh, J.; Choi, S.H.; Kim, H.; et al. Lithio-amphiphilic nanobilayer for high energy density anode-less all-solid-state batteries operating under low stack pressure. *Energy Environ. Sci.* **2024**, *17*, 7932–7943. <https://doi.org/10.1039/D4EE03130J>.
112. Cao, D.; Ji, T.; Wei, Z.; et al. Enhancing Lithium Stripping Efficiency in Anode-Free Solid-State Batteries through Self-Regulated Internal Pressure. *Nano Lett.* **2023**, *23*, 9392–9398. <https://doi.org/10.1021/acs.nanolett.3c02713>.
113. Kim, K.H.; Lee, M.-J.; Ryu, M.; et al. Near-strain-free anode architecture enabled by interfacial diffusion creep for initial-anode-free quasi-solid-state batteries. *Nat. Commun.* **2024**, *15*, 3586. <https://doi.org/10.1038/s41467-024-48021-w>.

114. Ma, S.; Zhao, J.; Xiao, H.; et al. Modulating the Inner Helmholtz Plane towards Stable Solid Electrolyte Interphase by Anion- π Interactions for High-Performance Anode-Free Lithium Metal Batteries. *Angew. Chem. Int. Ed.* **2024**, *137*, e202412955. <https://doi.org/10.1002/anie.202412955>.
115. Becker, J.; Fuchs, T.; Ortmann, T.; et al. Microstructure of Lithium Metal Electrodeposited at the Steel|Li6PS5Cl Interface in “Anode-Free” Solid-State Batteries. *Adv. Energy Mater.* **2024**, *2404975*. <https://doi.org/10.1002/aenm.202404975>.
116. Li, R.; Jiang, D.; Du, P.; et al. Negating Na|Na₃Zr₂Si₂PO₁₂ interfacial resistance for dendrite-free and “Na-less” solid-state batteries. *Chem. Sci.* **2022**, *13*, 14132–14140. <https://doi.org/10.1039/D2SC05120F>.
117. Hu, A.; Chen, W.; Li, F.; et al. Nonflammable Polyfluorides-Anchored Quasi-Solid Electrolytes for Ultra-Safe Anode-Free Lithium Pouch Cells without Thermal Runaway. *Adv. Mater.* **2023**, *35*, 2304762. <https://doi.org/10.1002/adma.202304762>.
118. Gu, D.; Kim, H.; Kim, B.-K.; et al. Chlorine-rich lithium argyrodite enables stable interfacial Li plating/stripping behavior in anode-free all-solid-state batteries. *CrystEngComm* **2023**, *25*, 4182–4188. <https://doi.org/10.1039/D3CE00560G>.
119. Liu, Y.; Meng, X.; Wang, Z.; et al. Development of quasi-solid-state anode-free high-energy lithium sulfide-based batteries. *Nat. Commun.* **2022**, *13*, 4415. <https://doi.org/10.1038/s41467-022-32031-7>.
120. Yin, Q.; Li, T.; Zhang, H.; et al. SEI/dead Li-turning capacity loss for high-performance anode-free solid-state lithium batteries. *J. Energy Chem.* **2024**, *96*, 145–152. <https://doi.org/10.1016/j.jechem.2024.04.033>.
121. Lu, Z.; Yang, H.; Wu, G.; et al. A “Liquid-In-Solid” Electrolyte for High-Voltage Anode-Free Rechargeable Sodium Batteries. *Adv. Mater.* **2024**, *36*, 2404569. <https://doi.org/10.1002/adma.202404569>.
122. Han, X.; Han, J.; Ma, K.; et al. A fluoride gradient, Zn-salt-rich hydrophobic interphase formed by a zincophilic, hydrophobic, anion-philic polymer “skin” for an anode-free solid Zn battery. *Energy Environ. Sci.* **2024**, *17*, 9244–9254. <https://doi.org/10.1039/D4EE01978D>.
123. Genovese, M.; Louli, A.J.; Weber, R.; et al. Measuring the Coulombic Efficiency of Lithium Metal Cycling in Anode-Free Lithium Metal Batteries. *J. Electrochem. Soc.* **2018**, *165*, A3321. <https://doi.org/10.1149/2.0641814jes>.
124. Louli, A.J.; Coon, M.; Genovese, M.; et al. Optimizing Cycling Conditions for Anode-Free Lithium Metal Cells. *J. Electrochem. Soc.* **2021**, *168*, 020515. <https://doi.org/10.1149/1945-7111/abe089>.
125. Louli, A.J.; Genovese, M.; Weber, R.; et al. Exploring the Impact of Mechanical Pressure on the Performance of Anode-Free Lithium Metal Cells. *J. Electrochem. Soc.* **2019**, *166*, A1291. <https://doi.org/10.1149/2.0091908jes>.
126. Zhou, C.; Samson, A.J.; Garakani, M.A.; et al. Communication—Anode-Free Lithium Metal Batteries: A Case Study of Compression Effects on Coin Cell Performance. *J. Electrochem. Soc.* **2021**, *168*, 060532. <https://doi.org/10.1149/1945-7111/ac0998>.
127. Genovese, M.; Louli, A.J.; Weber, R.; et al. Hot Formation for Improved Low Temperature Cycling of Anode-Free Lithium Metal Batteries. *J. Electrochem. Soc.* **2019**, *166*, A3342. <https://doi.org/10.1149/2.0661914jes>.
128. Gu, J.; Shi, Y.; Du, Z.; et al. Stress Relief in Metal Anodes: Mechanisms and Applications. *Adv. Energy Mater.* **2023**, *13*, 2302091. <https://doi.org/10.1002/aenm.202302091>.
129. Zhu, X.; Cheng, H.; Lyu, S.; et al. High-Energy-Heavy-Ion Engineering Low-Tortuosity and High-Porosity 3D Metallic Electrodes for Long-Life Lithium Anodes. *Adv. Energy Mater.* **2023**, *13*, 2300129. <https://doi.org/10.1002/aenm.202300129>.
130. Bazak, J.D.; Mueller, K.T.; Murugesan, V. Battery detectives: Uncovering cathode impact on anode-free Li cell performance by *operando* NMR. *Chem* **2024**, *10*, 2935–2937. <https://doi.org/10.1016/j.chempr.2024.09.009>.
131. Kwon, Y.; Svirinovsky-Arbeli, A.; Hestenes, J.C.; et al. Elucidating the role of cathode identity: Voltage-dependent reversibility of anode-free batteries. *Chem* **2024**, *10*, 3159–3183. <https://doi.org/10.1016/j.chempr.2024.06.008>.
132. Zhao, J.; Tang, M.; Lan, H.; et al. An anode-free sodium dual-ion battery. *Energy Storage Mater.* **2024**, *70*, 103480. <https://doi.org/10.1016/j.ensm.2024.103480>.
133. Wang, D.Y.; Sinha, N.N.; Petibon, R.; et al. A systematic study of well-known electrolyte additives in LiCoO₂/graphite pouch cells. *J. Power Sources* **2014**, *251*, 311–318. <https://doi.org/10.1016/j.jpowsour.2013.11.064>.
134. Lin, L.; Wang, J.; Li, R.; et al. Synergistic effect of interface layer and mechanical pressure for advanced Li metal anodes. *Energy Storage Mater.* **2020**, *26*, 112–118. <https://doi.org/10.1016/j.ensm.2019.12.039>.
135. Liu, L.; Yin, Y.-X.; Li, J.-Y.; et al. Uniform Lithium Nucleation/Growth Induced by Lightweight Nitrogen-Doped Graphitic Carbon Foams for High-Performance Lithium Metal Anodes. *Adv. Mater.* **2018**, *30*, 1706216. <https://doi.org/10.1002/adma.201706216>.
136. Qin, N.; Sun, Y.; Hu, C.; et al. Boosting high initial coulombic efficiency of hard carbon by in-situ electrochemical presodiation. *J. Energy Chem.* **2023**, *77*, 310–316. <https://doi.org/10.1016/j.jechem.2022.10.032>.
137. Chen, L.; Chiang, C.-L.; Wu, X.; et al. Prolonged lifespan of initial-anode-free lithium-metal battery by pre-lithiation in Li-rich Li₂Ni_{0.5}Mn_{1.5}O₄ spinel cathode. *Chem. Sci.* **2023**, *14*, 2183–2191. <https://doi.org/10.1039/D2SC06772B>.

138. Lin, L.; Qin, K.; Zhang, Q.; et al. Li-Rich $\text{Li}_2[\text{Ni}_{0.8}\text{Co}_{0.1}\text{Mn}_{0.1}]\text{O}_2$ for Anode-Free Lithium Metal Batteries. *Angew. Chem. Int. Ed.* **2021**, *60*, 8289–8296. <https://doi.org/10.1002/anie.202017063>.
139. Lin, L.; Qin, K.; Li, M.; et al. Spinel-related $\text{Li}_2\text{Ni}_{0.5}\text{Mn}_{1.5}\text{O}_4$ cathode for 5-V anode-free lithium metal batteries. *Energy Storage Mater.* **2022**, *45*, 821–827. <https://doi.org/10.1016/j.ensm.2021.12.036>.
140. Xu, T.; Qin, K.; Tian, C.; et al. Searching for the ideal $\text{Li}_{1+x}\text{TMO}_2$ cathode for anode-free Li metal batteries. *Energy Storage Mater.* **2025**, *74*, 103956. <https://doi.org/10.1016/j.ensm.2024.103956>.
141. Tian, C.; Qin, K.; Xu, T.; et al. Hybrid Li-rich cathodes for anode-free lithium metal batteries. *Next Nanotechnol.* **2025**, *7*, 100114. <https://doi.org/10.1016/j.nxnano.2024.100114>.
142. Wu, J.; Lin, C.; Liang, Q.; et al. Sodium-rich NASICON-structured cathodes for boosting the energy density and lifespan of sodium-free-anode sodium metal batteries. *InfoMat* **2022**, *4*, e12288. <https://doi.org/10.1002/inf2.12288>.
143. Golozar, M.; Hovington, P.; Paoletta, A.; et al. In Situ Scanning Electron Microscopy Detection of Carbide Nature of Dendrites in Li–Polymer Batteries. *Nano Lett.* **2018**, *18*, 7583–7589. <https://doi.org/10.1021/acs.nanolett.8b03148>.
144. Liang, X.; Pang, Q.; Kochetkov, I.R.; et al. A facile surface chemistry route to a stabilized lithium metal anode. *Nat. Energy* **2017**, *2*, 17119. <https://doi.org/10.1038/nenergy.2017.119>.
145. Liu, S.; Ji, X.; Piao, N.; et al. An Inorganic-Rich Solid Electrolyte Interphase for Advanced Lithium-Metal Batteries in Carbonate Electrolytes. *Angew. Chem. Int. Ed.* **2021**, *60*, 3661–3671. <https://doi.org/10.1002/anie.202012005>.
146. Liang, W.; Lian, F.; Meng, N.; et al. Adaptive formed dual-phase interface for highly durable lithium metal anode in lithium–air batteries. *Energy Storage Mater.* **2020**, *28*, 350–356. <https://doi.org/10.1016/j.ensm.2020.03.022>.
147. Zhang, W.; Sayavong, P.; Xiao, X.; et al. Recovery of isolated lithium through discharged state calendar ageing. *Nature* **2024**, *626*, 306–312. <https://doi.org/10.1038/s41586-023-06992-8>.